Title

Geomorphological analysis of the southwestern margin of Xanadu, Titan: Insights on tectonics

Authors

Pietro Matteoni[1], Giuseppe Mitri[1,2], Valerio Poggiali[3], Marco Mastrogiuseppe[4]

[1]International Research School of Planetary Sciences, Università d'Annunzio, Pescara, Italy

[2]Dipartimento di Ingegneria e Geologia, Università d'Annunzio, Pescara, Italy

[3]Department of Astronomy, Cornell University, Ithaca, NY, USA

[4] Dipartimento di Ingegneria dell'Informazione, Elettronica e Telecomunicazioni (DIET), Sapienza Università di Roma, Rome, Italy

Corresponding author: Pietro Matteoni (pietro.matteoni@unich.it)

Key Points

- Detailed geomorphological mapping of southwestern Xanadu has been conducted, using radar and newly available topographic data
- Several putative tectonic structures have been identified in this area of Titan
- Southwestern Xanadu is interpreted as a pull-apart basin formed by transtensional tectonic activity

Abstract

Evidence for tectonic activity on Titan is provided by the presence of eroded mountain ranges. Xanadu is an equatorial region of Titan characterized by a complex topography, even though overall it has a lower average elevation compared to its surroundings. We investigated Xanadu's southwestern margin, a part of the region which is comprised of heavily eroded and rugged terrains to the north and east and of smoother, more uniform terrains to the west and south. The central portions of southwestern Xanadu are characterized by an extensive fluvial network. The presence of such a distinctive feature was the main reason motivating the study of this area, given its potential to provide tectonic indications. Through detailed geomorphological mapping (map scale 1:700,000) on Synthetic Aperture Radar (SAR) data and analysis of both fluvial drainage patterns and Digital Terrain Models (DTMs), we identified several putative tectonic structures in this area: normal faulting to the west and east, thrust faulting to the north, small-scale strike-slip faulting in its central parts. Pull-apart basins are depressions bounded by both dip-slip faults and by (overlapping and/or bending) segments of a major transcurrent fault, i.e., they are basins generated in transtensional tectonic settings. We propose that central southwestern Xanadu is a pull-apart basin, bordered by both normal and thrust faults and formed by transtensional tectonics, which we consider to be the most recent tectonic phase active in this area. This basin is characterized by small-scale strike-slip faulting within it, on which a fluvial network has subsequently imposed.

Plain Language Summary

Saturn's largest moon, Titan, has several mountain ranges on its surface. It is thought that they are formed by large-scale processes related to Titan's interior. Xanadu is an equatorial region characterized by a rugged topography, even though its surrounding regions stand higher. We investigated Xanadu's southwestern margin, which is characterized by many different terrain types and by the presence of a hydrocarbon-related fluvial system. At Titan's surface pressure and temperature, hydrocarbons are in a liquid state and can therefore form rivers. Using radar data from

the Cassini mission, we mapped in detail the differences in morphology of each terrain in the region. Combining these results with those derived from analysis of sparsely available Cassini's elevation data, we identified several areas that may testify of the influence of Titan's internal processes on shaping the region.

1. Introduction

Saturn's largest moon, Titan, is currently identified as one of the few extra-terrestrial bodies whose surface supports standing liquid bodies. It is also considered, along with Earth and early Mars, as one of the three Solar System bodies to have had an active hydrologic cycle (Hayes, 2016; Hayes et al., 2018). Furthermore, Titan's atmosphere is the second densest amongst the terrestrial planets and icy satellites. Present day surface–atmosphere interactions make aeolian, fluvial, pluvial and lacustrine processes prominent on a scale seen only on Earth (Lopes et al., 2010, 2020) The satellite's atmosphere consists mainly of nitrogen (N_2 ~97%), methane (CH_4 ~1.4% in the troposphere, 5% at the surface) and hydrogen (H_2 ~0.2%) with traces of more complex hydrocarbons, nitriles, oxygen compounds and argon as analyzed by the Huygens probe (Coustenis et al., 2010; Coustenis, 2005; Dalton et al., 2010). Under Titan's surface conditions (pressure ~1.5 bars; temperature ~91–95 K), methane (CH_4) and ethane (C_2H_6) are both able to condense out of the atmosphere and precipitate to the surface, where the fluid runoff concentrates, incises channels and transports sediment (Birch et al., 2017; Hayes et al., 2018; Jaumann et al., 2008; Lorenz et al., 2008; Lunine & Lorenz, 2009).

Moreover, landforms similar to those common on Earth are found on Titan, including lakes and seas (Hayes et al., 2008; Mastrogiuseppe et al., 2018; Mitri et al., 2007, 2019; Stofan et al., 2007) dunes fields, with individual dunes up to hundreds of meters in height (Lorenz et al., 2006; Malaska, Lopes, Hayes, et al., 2016; Mastrogiuseppe et al., 2014; Neish et al., 2010; Radebaugh et al., 2008), impact craters (Elachi et al., 2006; Neish & Lorenz, 2012; Stofan et al., 2006; Werynski et al., 2019; Wood et al., 2010), fans and deltas (Birch et al., 2016; Cartwright & Burr, 2017; Radebaugh et al.,

2016; Witek & Czechowski, 2015) and mountains (Barnes, Radebaugh, et al., 2007; Cook-Hallett et al., 2015; Liu, Radebaugh, Harris, Christiansen, Neish, et al., 2016; Mitri et al., 2010; Moore & Pappalardo, 2011; Radebaugh et al., 2007). Moreover, fluvial channels and valleys related to a hydrocarbon cycle on Titan have been identified all over the surface at many different latitude ranges, apart from areas dominated by dune fields (Black et al., 2017; Burr et al., 2009; Burr, Perron, et al., 2013; Cartwright et al., 2011; Le Gall et al., 2010; Hayes, 2016; Hayes et al., 2018; Jaumann et al., 2008; Langhans et al., 2012; Lopes et al., 2020; Lorenz et al., 2008; Maue & Burr, 2018; Perron et al., 2006; Radebaugh et al., 2016; Reid et al., 2018; Tewelde et al., 2013). Such characteristics make Titan an ideal laboratory to study and compare terrestrial and planetary landscape-shaping processes (Hayes, 2016), although its landforms have all been formed and developed under very different environmental and physical conditions in comparison to Earth (Birch et al., 2017; Lorenz et al., 2008; Stofan et al., 2006).

A consensus is shared on the presence of a subsurface ocean on Titan (Iess et al., 2012; Lunine, 2017; Mitri et al., 2010, 2014; Nimmo, 2018; Stern et al., 2018). Due to its orbital eccentricity value (e = 0.028) Titan is subject to a large variability of tidal force intensities along its 16-day orbit around Saturn (Iess et al., 2012). Analysis of its response to the varying external gravity field has demonstrated the presence of a global subsurface ocean, likely lying above high-pressure ices (ice V, VI), which decouples an ice I shell (supposed to have a thickness of 70-100 km) from the deeper interior (Mitri et al., 2010, 2014). Such ocean should have a high salinity, as a result of its inferred relatively high density (Mitri et al., 2014), which was in turn derived from the measured tidal Love number, $k_2 = 0.589 \pm 0.150$ (Iess et al., 2012). Tidal heating does not play a big role on Titan, since it is not in orbital resonance with other satellites; therefore, the primary thermal energy source should be a progressively decreasing heat flux, due to radiogenic decay. This preserves the existence of the ocean through geological time but results in gradual global cooling (Mitri et al., 2010; Tobie et al., 2006). The progressive freezing of the ocean generates thickening of both the ice I shell and the high-pressure ices layer, the latter expected to be present at the base of the ocean. Concurrently, the

assumed high salinity of the ocean should inhibit further refreezing. The simultaneous thickening of the ice I shell and of the high-pressure ices layer produces a global radial contraction on Titan, due to density differences among both the ice layers and the ocean (Mitri et al., 2010). The surficial expressions of such a compressive stress field would be long-wavelength folds and fold-and-thrust belts (Mitri et al., 2010). This model best explains the observed high elevation ridges (e.g., Liu, Radebaugh, Harris, Christiansen, & Rupper, 2016; Liu, Radebaugh, Harris, Christiansen, Neish, et al., 2016; Solomonidou et al., 2013). Still, it does not completely fit with the ridges' general orientation - east-west around the equator and north-south at high latitudes - which have been related to polar thinning of the outer ice shell (Cook-Hallett et al., 2015).

Therefore, evidence for tectonic activity on Titan is exemplified by the presence of eroded mountain ranges (Mitri et al., 2010; Radebaugh et al., 2007). Due to poor Synthetic Aperture Radar (SAR) resolution and paucity of low error range elevation data (i.e., Cassini's Radio Detection And Ranging Instrument – RADAR – altimetry) tectonic indicators on Titan might be identified by indirect approaches (Liu, Radebaugh, Harris, Christiansen, & Rupper, 2016) such as analysis of drainage networks' azimuths (Burr et al., 2009; Burr, Drummond, et al., 2013) and planform geometries (e.g., width function, channel sinuosity, distribution and orientation of mountain ridges; Black et al., 2012; Liu, Radebaugh, Harris, Christiansen, Neish, et al., 2016). Amongst others, surface expressions that would be strongly indicative of tectonic activity on Titan are pull-apart basins. These are depressions bounded by both dip-slip faults and by (overlapping and/or bending) segments of a major transcurrent fault, i.e., they are basins generated in transtensional tectonic settings. Slip along the segments of the transcurrent fault results in extension of the region comprised between the fault segments (Gürbüz, 2010; Mann et al., 1983).

Xanadu is an equatorial landmass, extending for an area of about 4000 × 2500 km. It was first observed using the Hubble Space Telescope (Smith et al., 1996) and was retroactively detected in Voyager-1 optical images from 1980 (Richardson et al., 2004). It is the brightest (at all wavelengths) and largest geologic feature on Titan's surface. It is located on Titan's leading hemisphere and it

interrupts the sand seas (Barnes et al., 2015), which otherwise dominate the equatorial regions (Lopes et al., 2020). It has a generally high SAR brightness, indicating that it is made up of rugged terrains (Radebaugh et al., 2011). Xanadu's characteristics make it unique among Titan's regions and indicate a long and complex geological history: deeply eroded, incised, mountain ranges are carved by extensive fluvial networks emptying in fans to the south; linear features likely tectonic in nature are widespread, as well as impact craters, which are twice as common compared to the rest of Titan (Birch et al., 2016; Burr et al., 2009; Le Gall et al., 2010; Radebaugh et al., 2011; Wood et al., 2010). Despite the wide distribution of mountains and high local topographic variations, overall the region has a lower average elevation compared to its surroundings (Lopes et al., 2019; Radebaugh et al., 2011) as evident from RADAR altimetry data, SARTopo data, shape and topographic models, and Digital Terrain Models (DTMs) (Corlies et al., 2017; Kirk et al., 2012; Lorenz et al., 2013; Mitri et al., 2014; Stiles et al., 2009; Zebker et al., 2009). This represents Xanadu's most intriguing characteristic and brought several authors to study this region; yet, the origins of Xanadu remain enigmatic. Brown et al. (2011) suggested that the geomorphology of Xanadu is consistent with the site of an ancient impact, while Langhans et al. (2013) proposed that it is a remnant of past tectonic activity, reworked and resurfaced in recent times by fluvial processes. A detailed study of the Xanadu region, which further divides it into several units, is presented in Radebaugh et al. (2011). In contrast to Brown et al. (2011), these authors proposed that Xanadu has had a complex tectonic history, involving both compressional and extensional events. In a first tectonic phase, the region would have undergone crustal thickening via north-south directed regional scale compression. This phase would have had surface expressions such as oriented parallel mountain ridges (and related valleys) and fold-and-thrust belts. Subsequently an extensional event would have occurred, favored by slip along region-bounding faults, resulting in horst-and-graben-like structures. The extended fluvial network in southwestern Xanadu (henceforth, SW Xanadu) is argued (Burr et al., 2009; Burr, Drummond, et al., 2013) to have developed over a pre-existing east-west tectonic fabric (rectangular-type pattern), with a general

drainage direction from north to south. The tectonic style responsible for generating such a pattern is thought to be extensional, by analogy with terrestrial examples.

Previous geomorphologic works of Titan include global mapping (Lopes et al., 2010, 2016, 2020) and several regional maps (Birch et al., 2017; Malaska, Lopes, Williams, et al., 2016; Moore et al., 2014; Radebaugh et al., 2011; Williams et al., 2011). The present study aims at investigating southwestern Xanadu's formation and the related geological processes, through detailed geomorphological mapping (map scale 1:700,000) together with both qualitative and quantitative analysis of drainage patterns and DTMs. Compared to the global mapping (scale 1:20,000,000) of Lopes et al. (2020), the finer-scale geomorphological map presented in this work distinguishes among 10 units and subunits in SW Xanadu, while Lopes et al. (2020) differentiated between 5 units in the same area. The interpretation of said units is in agreement with that presented here.

2. Methods

A geomorphological map of SW Xanadu was produced (Figure 1b) based on Cassini's SAR images (spatial resolution: ~350 m; Elachi et al., 2004), which were imported in various Geographical Information System (GIS) environments along with topographic data in the form of SARTopo (vertical resolution: ± 150 m, horizontal resolution: ~10 km; Stiles et al., 2009) and DTMs processed through stereophotogrammetry (vertical resolution: ± 100 m, horizontal resolution: ~1400 m, the co-registration accuracy is similar to the spatial resolution of SAR data; (Kim et al., 2016; Kirk et al., 2008, 2012; Kirk & Howington-Kraus, 2008). DTMs are available only in sparsely distributed areas of SAR swath overlap. Other mentioned Cassini's datasets, yet not directly analyzed, include those of other RADAR modes, such as HiSAR (high-altitude, lower resolution SAR) and radiometry (measurement of natural thermal emission; Janssen et al., 2009), along with ISS (Imaging Science Subsystem, v-nIR camera; Porco et al., 2004) and VIMS (Visual and Infrared Mapping Spectrometer; Brown et al., 2004). All datasets have been projected using the same reference system (equidistant

cylindrical projection) centered at 0°N, 0°E. Mapping was conducted at a spatial scale of 350 m/pixel (SAR resolution), which corresponds to a map scale of 1:700,000.

In this work, the interpretation of surface geomorphology has been the main technique used to characterize the hypothesized surficial expressions of Titan's tectonism. Distinction among different geomorphological units has been conducted manually and is based on: SAR backscatter characteristics, morphology, topographic relationship (based on SARTopo and DTMs data, where available), internal texture and contact relations (Lopes et al., 2020; Williams et al., 2011). In compliance with the guidelines given by Elachi et al. (2004), Ford et al. (1993) and Stofan et al. (2008), Titan's SAR dataset has been interpreted considering SAR's backscatter coefficient σ_0 values (range in linear scale: $0.1 \leq \sigma_0 \leq \sim 1.5$; classified as "high": $\sim 1 \leq \sigma_0 \leq \sim 1.5$, "medium": $\sim 0.5 \leq \sigma_0 \leq \sim 1$, "low": $\sim 0.1 \leq \sigma_0 \leq \sim 0.5$, or "variable"), which depend on: local incidence angle, surface roughness, volume scattering and dielectric properties (Cook-Hallett et al., 2015; Elachi et al., 2004; Ford et al., 1993; Lopes et al., 2010; Malaska, Lopes, Williams, et al., 2016; Williams et al., 2011). A network of linear features interpreted as fluvial valleys (Section 3.1.8) have been identified and their azimuths are investigated via rose diagrams analysis (Figure 2a). Furthermore, several linear structures interpreted as strike-slip faults (Section 3.2.1) have been analyzed via rose diagrams (Figure 2b).

3. Results

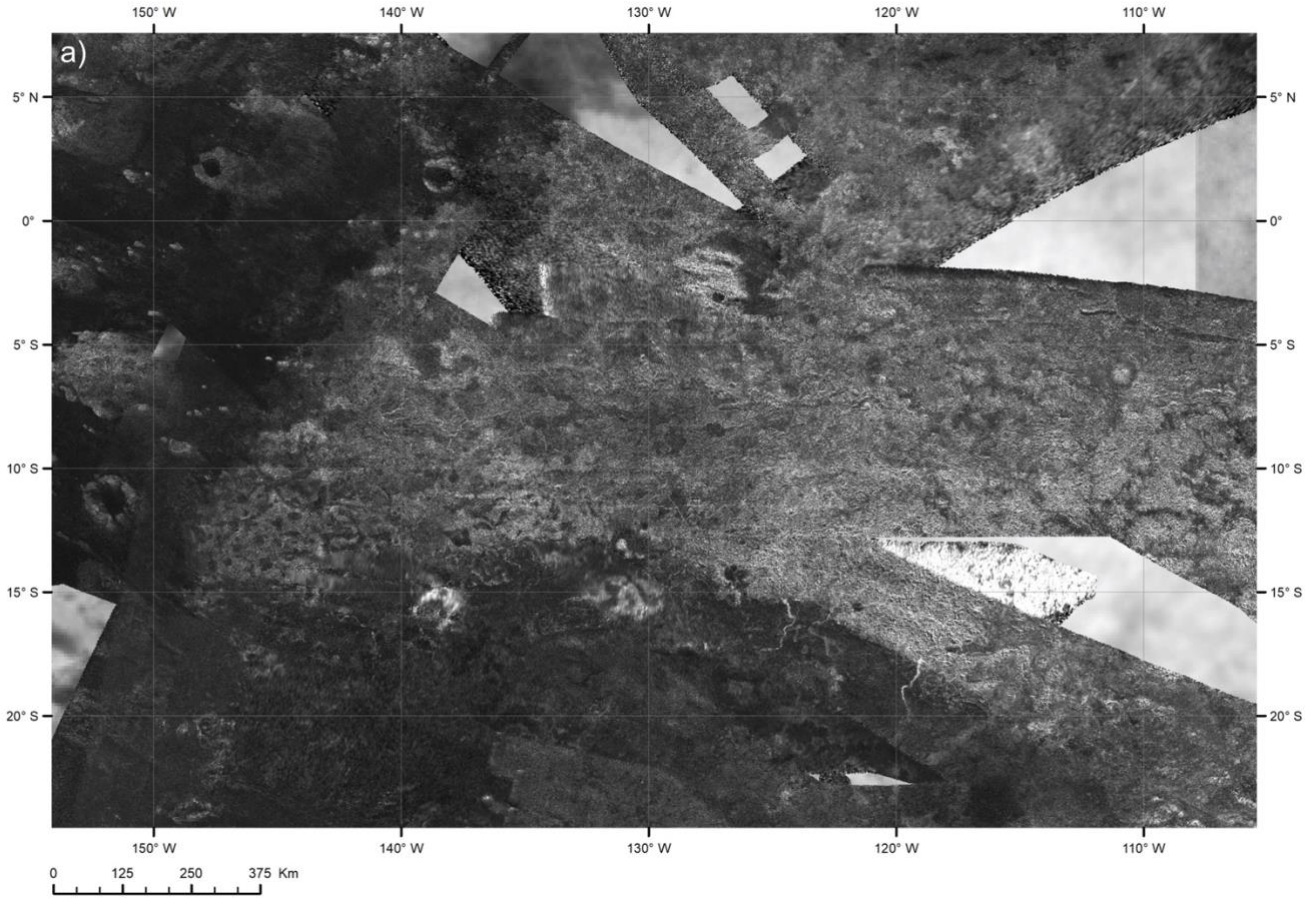
a)
150° W
140° W
130° W
120° W
110° W
5° N
0°
5° S
10° S
15° S
20° S
0
125
250
375 Km

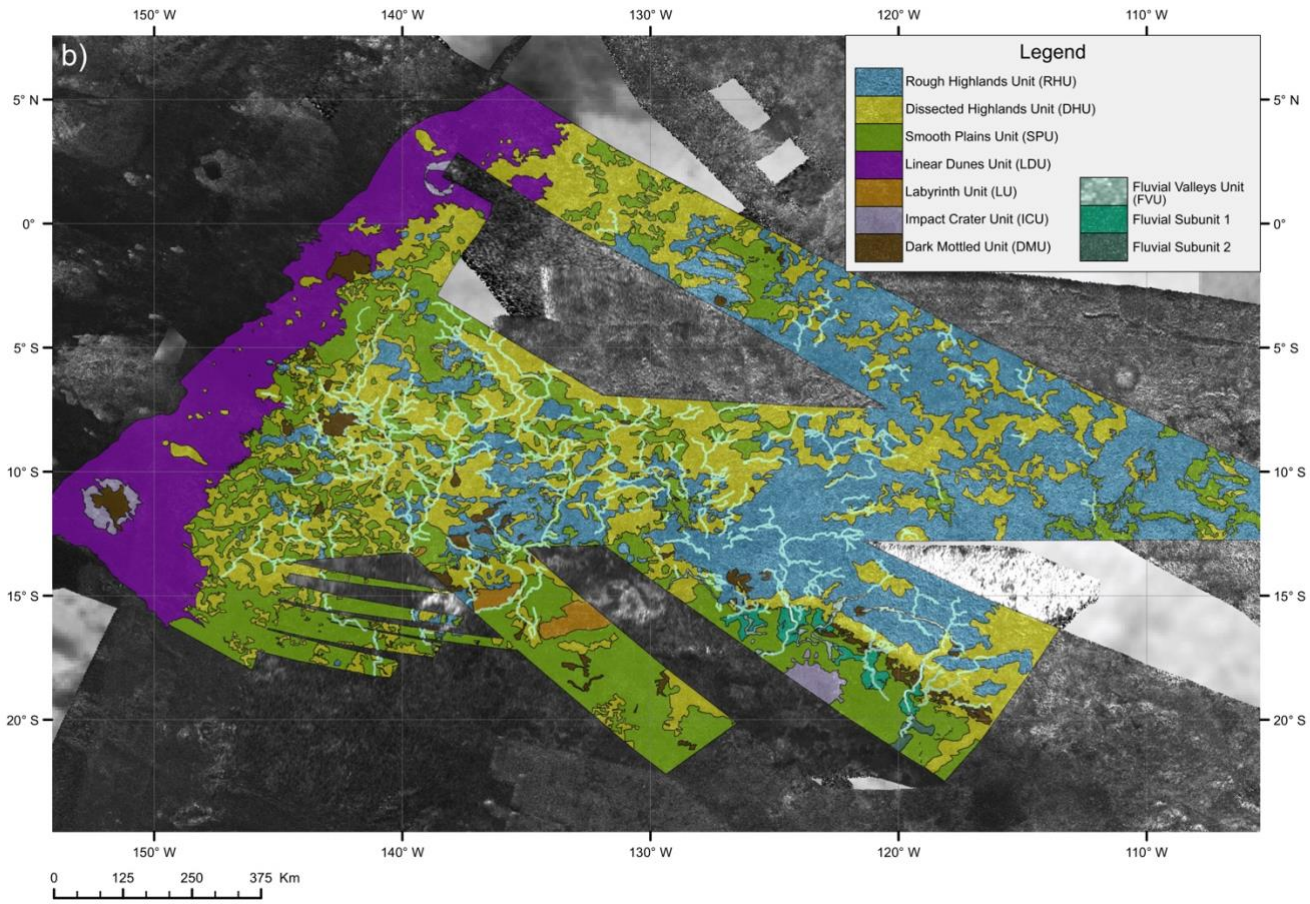
b)
Legend
Rough Highlands Unit (RHU)
Dissected Highlands Unit (DHU)
Smooth Plains Unit (SPU)
Linear Dunes Unit (LDU)
Labyrinth Unit (LU)
Impact Crater Unit (ICU)
Dark Mottled Unit (DMU)
Fluvial Valleys Unit (FVU)
Fluvial Subunit 1
Fluvial Subunit 2
150° W
140° W
130° W
120° W
110° W
5° N
0°
5° S
10° S
15° S
20° S
0
125
250
375 Km

198

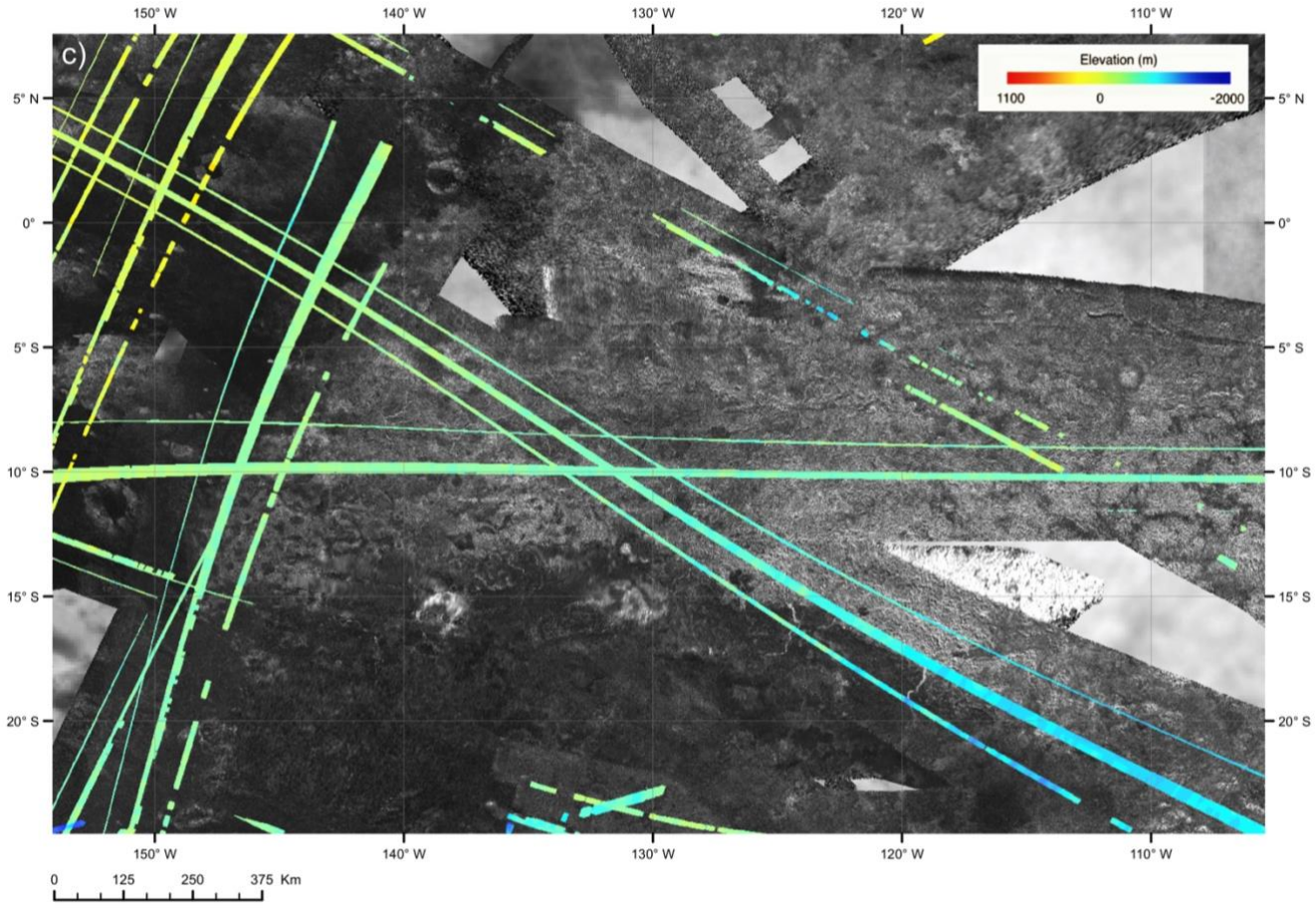
c)
Elevation (m)
1100
0
-2000
150° W
140° W
130° W
120° W
110° W
5° N
0°
5° S
10° S
15° S
20° S
0
125
250
375 Km

199

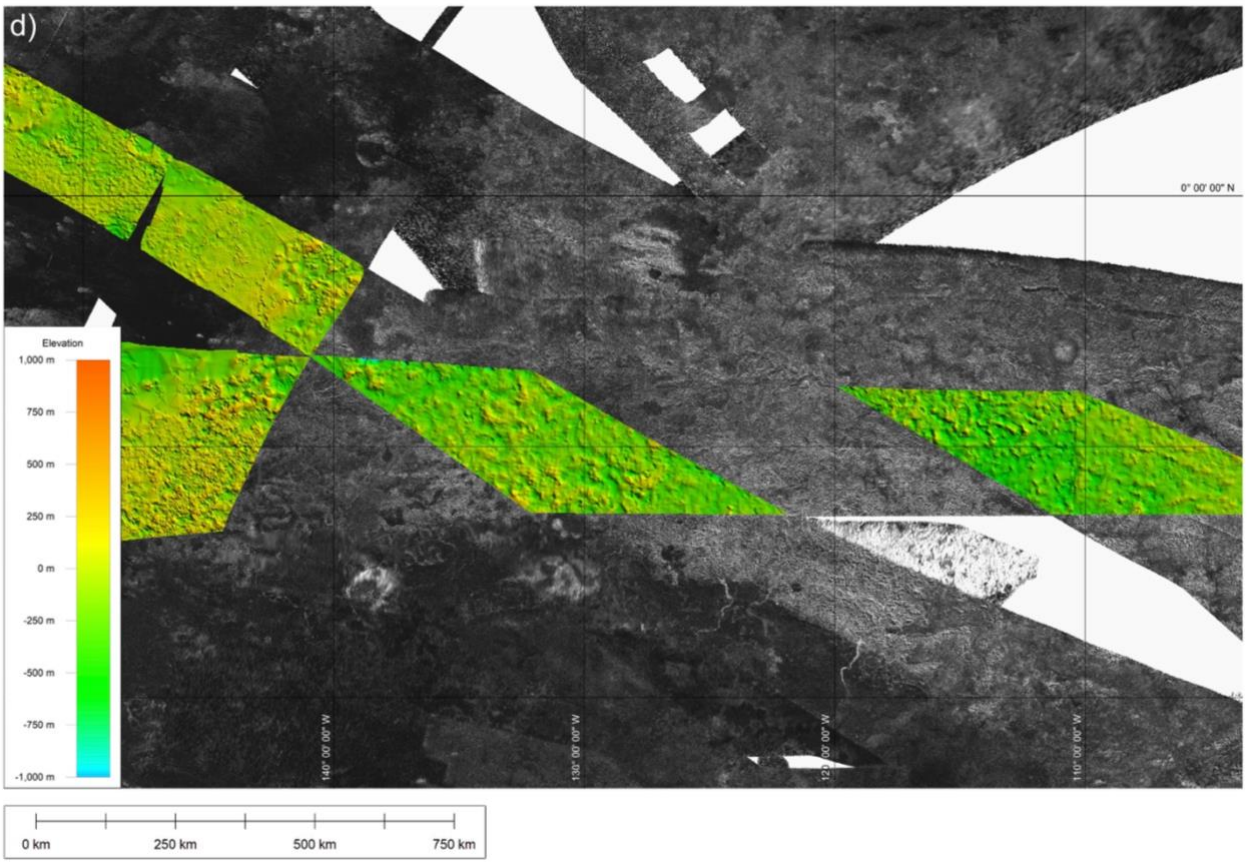
d)
0° 00' 00" N
Elevation
1,000 m
750 m
500 m
250 m
0 m
-250 m
-500 m
-750 m
-1,000 m
140° 00' 00" W
130° 00' 00" W
120° 00' 00" W
110° 00' 00" W
0 km
250 km
500 km
750 km

200

Figure 1. a) SAR images mosaic of southwestern Xanadu. **b)** Geomorphological map of southwestern Xanadu. The units' legend is displayed in the top-right corner. Some inner parts were not mapped, due to non-availability of SAR images at 350 m/pixel (or to the availability of HiSAR data, only). **c)** SARTopo mosaic overlain on SAR mosaic. **d)** DTMs overlain on SAR mosaic, in 2D visualization. Hillshading is enabled, with a vertical exaggeration factor of 5.
North is up and the area shown is the same in each panel. In panels a, b and c an ISS mosaic is used as background.

The main outcome of this study is a geomorphological map of southwestern Xanadu, based on Cassini's SAR images (Figure 1a), shown in Figure 1b. The mapping area has been determined in order to include the whole extension of the fluvial drainage network and of relevant elevation data (SARTopo and DTMs, Figure 1c-d), which have been used to derive topographic relationships. Hereafter follows a detailed definition, description and interpretation of the mapped geomorphological units.

3.1 Geomorphological Units Description and Interpretation

3.1.1 Rough Highlands Unit (RHU)

Rough Highlands Unit (RHU, marked in blue; Figure 1b and Sup. Figure 1b) is characterized by a generally high σ_0, yet with an observable widely distributed bright/dark pairing. It is comprised by linear ridges or irregular patches, always embayed by SAR-darker materials. In the mapped area it is the brightest unit, whereas its texture is intensely rugged and dissected (Sup. Figure 1a-b). Topographic data show how the RHU usually coincides with the highest elevations (values > 300 m, Figure 1c-d). Similar observations on a global scale led to the interpretation that this unit consists of mountainous terrains composed of icy bedrock (Barnes, Radebaugh, et al., 2007; Radebaugh et al., 2007). The high σ_0 most probably depends on high surface roughness and possible volume scattering

from the near subsurface (Janssen et al., 2011, 2016), while the bright/dark pairing SAR appearance may be due to different orientations of the slopes (Cook-Hallett et al., 2015; Elachi et al., 2006; Moore et al., 2014; Radebaugh et al., 2007).

The overall morphology of this unit is distinctive of ridges eroded by the exogenous agents, whose action results in the typical rugged and dissected, crenulated SAR texture (Jani Radebaugh et al., 2007). Considering the unambiguous theoretical and observational constraints, similar interpretations have been given by previous geomorphological studies on different regions of Titan (Birch et al., 2017; Lopes et al., 2010; Malaska, Lopes, Williams, et al., 2016; Williams et al., 2011).

3.1.2 Dissected Highlands Unit (DHU)

Dissected Highlands Unit (DHU, marked in yellow; Figure 1b and Sup. Figure 1d) has variable σ_0, ranging from medium-high to medium-low (Sup. Figure 1c). It is comprised of mottled and dissected patches, usually surrounding the RHU through quite abrupt boundaries (Sup. Figure 1d). The main discriminant between the two units is a relatively well distributed and homogenous "grainy" texture of the DHU. The analysis of topographic data has shown how the DHU elevation is variable but generally high (typical elevation values > 100-150 m, Figure 1c-d) compared to the other units, yet lower than the RHU (< 300 m, Figure 1c-d).

The DHU is interpreted as the result of the erosional breakdown of mountainous terrains, mainly by fluvial erosion and flank deposition (Aharonson et al., 2013; Lopes et al., 2010). These processes produce SAR brightness variations (i.e., the "grainy" texture previously mentioned), which are likely dominated by changes in surface roughness, volume scattering and compositional variations.

3.1.3 Smooth Plains Unit (SPU)

Smooth Plains Unit (SPU, marked in green; Figure 1b and Sup. Figure 1f) is formed by deposits of medium-low σ_0 material, with relatively homogenous appearance (Lopes et al., 2016). It tends to have gradational boundaries and occurs in patches that are generally hundreds of km in extent (Sup. Figure

1e). It is a unit typical of topographically depressed areas (typical elevation values < 0 m, Figure 1c-d), surrounded by the RHU and DHU (Sup. Figure 1f). It is composed of SAR-dark materials, probably of organic origin, as suggested by the VIMS results of Lopes et al. (2016) and Solomonidou et al. (2018), resulting either from fluvial deposition or from the accumulation of photolysis products created in the upper atmosphere (Aharonson et al., 2013; Lopes et al., 2016). Morphologically, the SPU comprises small basins and widespread plains, while most of the inferred fluvial valleys (FVU, Section 3.1.8) lie on this unit. Therefore, the SPU pre-dates the formation of the FVU features (see also Burr, Perron, et al., 2013).

3.1.4 Linear Dunes Unit (LDU)

Linear Dunes Unit (LDU, marked in purple; Figure 1b and Sup. Figure 1h) is formed by parallel to subparallel low σ_0 lineations on a variable σ_0 substrate. SAR-bright lineations can sometimes be seen coincident with dark ones, along an east-west or southwest-northeast strike (Sup. Figure 1g). Where present, LDU terrains embay inferred topographic barriers, diverting around these, or sometimes arresting at their contact (Figure 1b). Tapering relative relationships are also locally observed (Sup. Figure 1h). Topography across this and other Titan's regions has shown that the LDU terrains are not flat as they have rises and falls (common height difference between dune crest and trough in the order of ~60-120 m, Lorenz et al., 2006; Mastrogiuseppe et al., 2014). In the mapped area outcrops of RHU and DHU are often locally higher than the LDU, which has typical elevations values of -100 to 100 m (Figure 1c-d).

Linear dunes seas on Titan have been well characterized in the literature (e.g., Lorenz et al., 2006; Radebaugh et al., 2008; Radebaugh, 2013; Rodriguez et al., 2014). Williams et al. (2011) described these terrains as longitudinal dunes composed of fine-grained fragmental material deposited by aeolian processes. Microwave emissivity measurements show how dunes have a high emissivity. ISS images of these areas are dark at 0.93 µm and correspond to the VIMS *dark brown unit* (Barnes, Brown, et al., 2007; Janssen et al., 2009; Rodriguez et al., 2014). Both microwave emissivity and

infrared characteristics of the linear dunes are consistent with a composition of organic materials (Barnes et al., 2008; Le Gall et al., 2011; Janssen et al., 2009, 2016; Rodriguez et al., 2014). The coincident SAR-bright lines sometimes observed are consistent with specular reflections off a dune crest, when the incidence angle of the radar matches that of the dune crest (Malaska, Lopes, Williams, et al., 2016). Alternatively, this effect could be due to compositional heterogeneity between dunes and interdunes (Bonnefoy et al., 2016; Callegari et al., 2014).

3.1.5 Labyrinth Unit (LU)

Labyrinth Unit (LU, marked in orange; Figure 1b and Sup. Figure 2f) presents very dissected terrains, generally with medium σ_0, even though clear bright–dark pairing in the up range-down range side is evident (Sup. Figure 2e).

This unit is interpreted (Lopes et al., 2020; Malaska et al., 2020; Malaska, Lopes, Williams, et al., 2016; Moore et al., 2014) as uplands with canyons or valleys containing radar-dark floors or fill (Sup. Figure 2f), i.e., as dissected *plateaux* (due to generally high elevations) or remnant ridges of eroded organic materials that then release such materials into the plains and downstream basins.

3.1.6 Impact Craters Unit (ICU)

As previously mentioned, Titan has some recognizable impact craters on its surface. Craters can be discriminated from the adjacent units by a distinctive circular morphology (the rim), in most cases as high in σ_0 as the RHU, which usually encloses a medium-low σ_0 area (the crater floor) and may be surrounded by medium-high σ_0 ejecta material (Bottke & Norman, 2017; Hedgepeth et al., 2020; Neish et al., 2016; Neish & Lorenz, 2012; Wood et al., 2010). We classified the features that matched this description as Impact Craters Unit (ICU, marked in pink; Figure 1b and Sup. Figure 2b). In two cases (11°S; 152°W and 2°N; 138°W), we encountered features already classified as impact craters, with IAU nomenclature: “Guabonito” and “Veles”, respectively. For Guabonito, what is surrounded by the rim is inferred to be filling material, which may include bedrock exposed during impact and,

more likely, organics later emplaced by atmospheric airfall and aeolian processes (Werynski et al., 2019). In one other case (around 18°S; 123°W), two small patches of medium σ_0 are identified nearby a semi-circular (incomplete observation due to lack of SAR images at 350 m/pixel) main feature of medium to high σ_0 (Sup. Figure 2a).

In the latter case, the main feature is interpreted as a possible impact crater's outer rim (Lopes et al., 2010) and relative crater floor. The aforementioned two small patches are interpreted as crater ejecta, deposited as a consequence of the energetic impact event. However, this interpretation is limited by the absence of SAR images at 350 m/pixel on half of the main feature.

According to Werynski et al. (2019), craters in the equatorial dune fields have (when viewed with a color scheme of blue = 1.28 μm, green = 2 μm, and red = 4.8–5.2 μm) VIMS *bright green* ejecta and rims (suggestive of mixture of organics and water ice). All the above subunits (crater rim, floor and ejecta) have not been distinguished from each other using different identification colors, as it is not directly relevant to the main aim of this work and are thus joined in the ICU (Sup. Figure 2b).

3.1.7 Dark Mottled Unit (DMU)

Dark Mottled Unit (DMU, marked in brown; Figure 1b and Sup. Figure 2d) is the unit with the lowest local σ_0. It occurs in small irregular patches of lobate to mottled and angular morphologies (Sup. Figure 2c).

The DMU has been previously interpreted as low elevation localized basins dampened by liquid hydrocarbons or other damp materials (Hayes et al., 2008; Malaska, Lopes, Williams, et al., 2016; Neish & Lorenz, 2014), which however do not contain deep lakes of liquid hydrocarbons as observed at the north pole (Mastrogiuseppe et al., 2019). Their σ_0 is indeed not as low as for the liquid-filled polar lakes. Alternatively, finer grained materials could be contained within these basins, or materials that have less organized structure (thus less backscatter) on the surface or in the near subsurface (Janssen et al., 2011) than the surrounding terrain (Malaska, Lopes, Williams, et al., 2016) (Sup. Figure 2d).

Elevation data confirm how unit's patches correspond to local topographic lows all around the investigated area (typical elevation values < -100 m, Figure 1c-d). It can be further observed that the DMU is often found at the onset or end of fluvial units and may then represent local basins and/or fluvial headwaters. In very rare cases this unit exhibits the typical fan morphology, in proximity of inferred fluvial valleys. These isolated patches could then be examples of Titan's alluvial fans (Birch et al., 2016; Cartwright & Burr, 2017; Radebaugh et al., 2016).

3.1.8 Fluvial Valleys Unit (FVU)

Fluvial Valleys Unit (FVU, marked in light blue; Figure 1b and Sup. Figure 2h) is characterized by wide (~1-6 km), long (up to ~200-300 km), rough, sinuous, SAR-bright features; widths often vary noticeably along-distance (Sup. Figure 2g). The wider ends terminate and lie on SAR-dark terrain, mainly SPU, while the narrower ends reach SAR-bright terrain, usually RHU (Sup. Figure 2h).

Considering the hydrocarbon cycle ongoing on Titan some landform that contains the surficial liquid's runoff must exist, at locations where the substrate is not too porous (Coustenis, 2005; Hayes et al., 2008; Hayes, 2016). Furthermore, Huygens' DISR instrument imaged branched lineations and rounded cobbles around the Huygens Landing Site (10.6°S; 191°W), the only location on Titan's surface where observations have been made *in situ* (Perron et al., 2006; Tomasko et al., 2005). These have been interpreted, respectively, as fluvial valley networks with inset streams formed by flowing methane and as material transported by flowing liquid. This hypothesis is mainly determined by analogy with Earth's fluvial processes (Burr, Drummond, et al., 2013; Burr, Perron, et al., 2013; Perron et al., 2006; Tomasko et al., 2005). Orbital data (RADAR, VIMS, ISS) have also shown networked lineations, distributed at different latitudes. These have been interpreted as fluvial channels (Barnes, Radebaugh, et al., 2007; Brown et al., 2004; Elachi et al., 2006; Porco et al., 2005). However, as the best resolution for such orbital data (SAR's ~350 m/pixel) is much coarser than DISR's images (~15-30 m/pixel), only the largest fluvial valleys (including the surrounding valley walls and their relative SAR-shadowing on the riverbed) are supposedly identified, while the smaller, most recent,

channels should not (Birch et al., 2017; Burr et al., 2009; Moore & Pappalardo, 2011). Therefore, the local features observed in this work have been interpreted as fluvial valleys and thus termed accordingly.

The distinctive high σ_0 of the FVU features is most probably due to an elevated density of icy rounded pebbles with size as large as or slightly larger than the RADAR wavelength (2.18 cm). The pebbles' internal reflections would cause the observed high backscatter (Le Gall et al., 2010). Regarding the FVU features located around 17°S; 123°W, the observed decrease in width and SAR brightness with distance may be due to evaporation, abrasion (mechanical weathering) and/or infiltration over the SPU (Sup. Figure 2g). Alternatively, the change in appearance (brighter upstream, darker downstream) may result from selective sorting as the slope drops and the flow is less confined, i.e., more fine-grained materials (SAR-darker, as their size is smaller than the RADAR wavelength) are able to be transported towards the tip of the fluvial valley (Burr, Drummond, et al., 2013; Le Gall et al., 2010; Maue & Burr, 2018; Radebaugh et al., 2016).

3.1.8.1 Fluvial Subunits

In some limited areas a differentiation among the FVU has been made. This resulted in two subunits, Fluvial Subunit 1 (marked in aquamarine; Figure 1b and Sup. Figure 2h) and Fluvial Subunit 2 (marked in dark green; Figure 1b and Sup. Figure 2h). Given their direct correlation with the FVU and very limited extent, these units have not been formally defined as constituting separate ones, yet they have been distinguished from the main unit by using a different mapping color. Their definition and significance are described in Section 3.2.1.

3.2 Geomorphology, tectonic indicators and topography

382 Figure 1b represents the geomorphological map of southwestern Xanadu, as a result of this study.
383 The Rough Highlands Unit (RHU) and Dissected Highlands Unit (DHU) are the prevalent
384 geomorphological units towards the inner portions of the region, north and east, while the Smooth
385 Plains Unit (SPU) dominates in the south and west. To the far west of the mapped area, the Linear
386 Dunes Unit (LDU) - part of the Shangri-La region - is widespread and surrounds a few patches of
387 DHU, Impact Crater Unit (ICU) and Dark Mottled Unit (DMU). Most of the units' boundaries in the
388 mapped area are either gradational or not easily distinguishable. The most abrupt contact is aligned
389 roughly NW-SE (from 20°S; 118°W to 15°S; 128°W) along a sharp linear feature (see Le Gall et al.,
390 2010; Radebaugh et al., 2011), with several unit boundaries located along it (Figure 1). Where
391 present, fluvial units (Fluvial Valleys Unit - FVU- and relative subunits) lie on all the other mapped
392 units and therefore incised them, at least during the last period of fluvial activity (which could be of
393 episodic nature, as reported e.g., by Lunine & Lorenz, 2009).
394 The fluvial network (marked as FVU in the geomorphological map, Figure 1b) in central SW
395 Xanadu seems to deviate from an hypothetical drainage direction that is driven *only* by the local
396 northwest-southeast topographic gradient: i.e., a drainage direction that would form a dendritic
397 pattern, see Twidale (2004). This effect is probably due to the imposition of the fluvial network on
398 some pre-existing E-W, SW-NE, NW-SE linear features, as outlined by the drainage system rose
399 diagram's results (Figure 2a). Eventually, this leads to a rectangular-type drainage pattern (Howard,
400 1967; Twidale, 2004) for the connected reaches of the fluvial network at SW Xanadu.
401

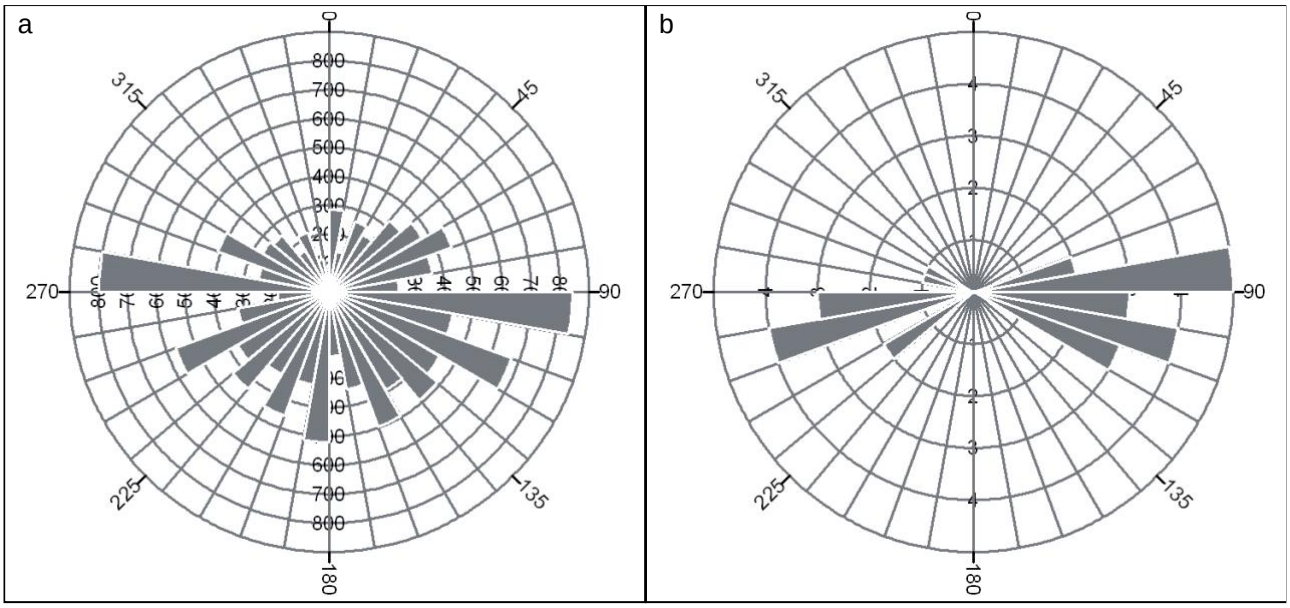

Figure 2. a) Azimuths of the connected reaches of the fluvial network at SW Xanadu, displayed in a unidirectional rose diagram (each segment of each valley is considered); the cumulative length of segments is shown divided into 10° bins. A segment constitutes the distance between two vertices in the FVU feature class, its surface coordinates (x_1, y_1 - x_2, y_2) are then calculated. The total population of valleys segments is 13,060. A broad, almost uniform, distribution of azimuths exists. The maximum population (843) is located in the 90°-100° bin (roughly east-west), while the mean value is along an east-west trend as well (93°). **b)** Azimuths of 28 linear features (examples shown on the map in Figure 4a-b), corresponding to abrupt changes in drainage direction of the fluvial network at SW Xanadu, displayed in a unidirectional rose diagram; the cumulative length of the segments is shown divided into 10° bins. The bins with the highest populations are 80°-90°, 100°-110°, 250°-260°.

Based on both SARTopo and DTMs, the overall average elevation values of SW Xanadu are between -500 m and 500 m (Figure 1c-d, Figure 3). This study mostly relied on DTMs, as their error range is lower, and they offer a wide spatial coverage on the area investigated, see Section 2. The

three topographic profiles shown in Figure 3 clearly expose how topographic peaks are present all over the mapped area, yet the average elevation decreases northwest to southeast (and west to east). Thus, both SARTopo and DTM data suggest the presence of a topographic gradient along these axes.

In Figure 3, going from A to B and from C to D along the topographic profiles, east of the Shangri-La dune field (from ~10°S; 142°W to ~3°S; 138°W; the mapped part of Shangri-La is mostly classified as LDU on the geomorphological map; Figure 1b), important local highs corresponding to RHU outcrops are identified (A to B: ~ +500 m at ~125 km; C to D: ~ +300 m at ~125 km). They are followed by distinct drops of hundreds of meters along sharp east-dipping slopes (A to B: ~ -500 m at ~150 km and ~ -250 m at ~200 km and at ~250 km; C to D: ~ -250 m at ~150 km and ~ -400 m at ~225 km) mainly corresponding to outcrops of DHU, SPU and DMU. In central SW Xanadu, which is dominated by fluvial features, the average elevation is lower compared to the previously mentioned areas to the west; the main topographic drops correspond to the widest fluvial valleys (FVU; Figure 1d, Figure 3). To the far east, the topography gradually increases again along a west-dipping block, as shown in the A-B and C-D topographic profiles in Figure 3 (from ~ 1500 km up to ~2000 km). In this part of the mapped area, a north-south striking linear feature is recognizable (centered at 10°S; 110°W; Figure 1, Figure 3). It extends for at least ~170 km and crosscuts two other similar features (centered at 9°S; 108°W and 11°S; 108°W, respectively, and both extending for ~150 km), which strike roughly NW-SE (dip direction ~200°W) parallel to each other and also to the aforementioned sharp linear feature located from 20°S; 118°W to 15°S; 128°W.

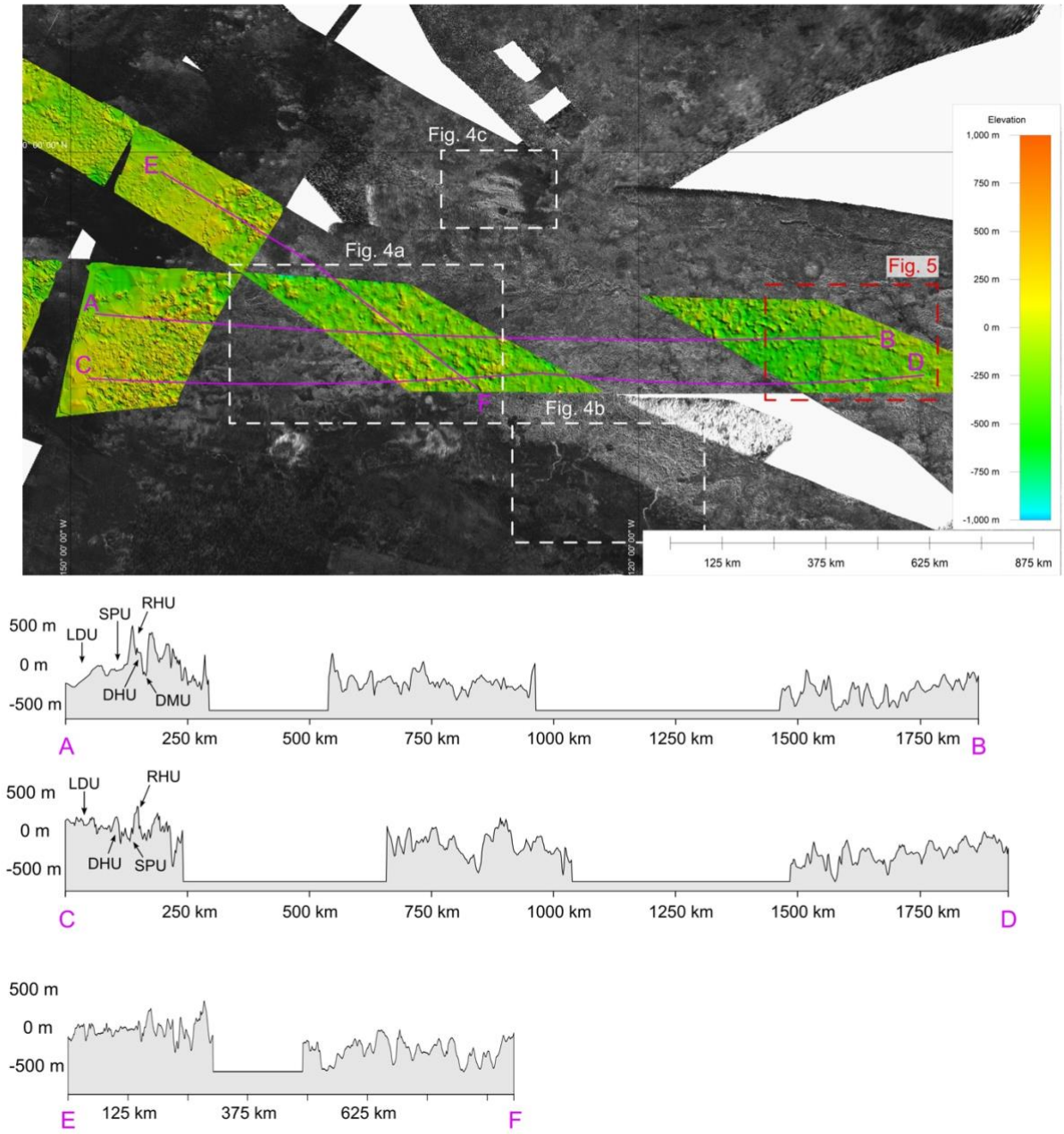

439

440

441 **Figure 3. Top)** DTMs overlain on SAR mosaic, in 2D visualization. Hillshading is enabled, with a
442 vertical exaggeration factor of 5. The areas shown are SW Xanadu and its surroundings, as in Figure
443 1. The white dashed polygons mark the areas shown in Figure 4. The red dashed polygon marks the
444 area shown in Figure 5. North is up. **Bottom)** Topographic profiles going from A to B and from C to
445 D, covering most of the mapped area (Figure 1b) from west to east. The topographic profile going
446 from E to F (northwest to southeast) crosscuts the A to B and C to D profiles. The A-B profile is also

447 shown in SW Xanadu's tectonic model in Figure 6. In the western parts of the A-B and C-D profiles,
448 the locations of several corresponding geomorphogical units' patches are shown. The sudden breaks
449 of the profiles are due to non-available DTM data in the corresponding locations.
450
451
452 **3.2.1 Interpretation**
453 This section provides interpretations of previously reported observations, which will only be repeated
454 when necessary.
455 Southwestern Xanadu is comprised of heavily eroded and rugged terrains to the north and east -
456 corresponding mainly to RHU and DHU - and of smoother and more uniform terrains to the west and
457 south - corresponding mainly to SPU and DMU. An extensive fluvial network is widespread,
458 particularly in the central portions of the examined area (Figure 1a-b).
459 The presence of liquid in the fluvial valleys would produce a distinctive SAR-darker backscatter
460 as it occurs at the polar rivers, lakes and seas (Birch et al., 2017; Hayes et al., 2008; Hayes, 2016;
461 Mastrogiuseppe et al., 2018; Mitri et al., 2007; Poggiali et al., 2016). Therefore, the observed
462 generally high backscatter of the mapped fluvial valleys probably implies that here, at the time of
463 Cassini's data acquisition, there was no detectable liquid runoff and these features just show remnants
464 of transported material (Le Gall et al., 2010). The potential for episodic fluvial activity (i.e.,
465 ephemeral) during infrequent rainfall events must although be considered (Lorenz, 2000; Lorenz et
466 al., 2008; Lunine & Lorenz, 2009). For fluvial networks characterized by many tributaries, as in SW
467 Xanadu, the drainage direction is mainly inferred by the direction of tributary confluence (Figure 1,
468 Figure 4a-b). The presence of downstream depositional sites such as basins/lakes/deltas and upstream
469 sources such as high-roughness terrains, can provide additional evidence to deduce the drainage
470 direction (Black et al., 2017; Burr, Drummond, et al., 2013; Maue & Burr, 2018). In the investigated
471 area, the upstream portions of the drainage basin are located to the north, corresponding to RHU and
472 DHU, whereas SPU and DMU and their surroundings represent the downstream portions of the

drainage basin to the south (Figure 1b). In its northern portions this fluvial network is embodied by narrower valleys, which tend to continue into wider ones to the south (mainly along the aforementioned sharp linear units' contact, Section 3.2) and then tend to narrow again with distance, towards their southern tips. This is particularly the case towards the SE of the mapped area, around 17°S; 123°W, where several sinuous wide fluvial features are identified: the SAR-brighter ones are thought to contain a higher amount of icy pebbles (Figure 1, Figure 4b). Such material would have been transported and rounded by stream flow, most likely by liquid hydrocarbons during flood events (see Section 3.1.8). Next to such features some morphologically similar ones, yet SAR-darker, are identified (e.g., 16°S; 123°W, 16°S; 127°W, Figure 1, Figure 4b). These are interpreted as remnants of abandoned rivers, which were active during a previous phase and were darkened *in situ* either by deposition of fine atmospheric precipitates or by size reduction of the icy pebbles, through a combination of mechanical (aeolian and/or rainfall weathering, although the generally slow wind speeds at these latitudes and slow rainfall rates must be taken into account; see e.g., Lunine & Lorenz, 2009; Tokano, 2010) and chemical weathering (Le Gall et al., 2010). Such interpretation may imply a fluvial system characterized by a high level of maturity, a hypothesis which is also supported by the large number of tributaries present at the higher portions of the drainage basin. At its downstream portions the fluvial network's maturity is suggested by the many putative meandering channels (see Birch et al., 2018; Burr, Perron, et al., 2013; Howard, 2009), which were grouped together in the Fluvial Subunit 1 (Figure 1a-b, Figure 4b). Eventually, a distinctive feature that morphologically resembles an Earth's river lobate delta was identified (20°S; 119°W; Figure 1a-b, Figure 4b). Such an hypothesis is supported by considering that this feature is found co-located with the SAR-darker portion (i.e., the tip of the fluvial valley, where particles get finer) of one of the most evident, bright fluvial valleys (see Witek & Czechowski, 2015), in an area of probable important topographic drop (see later in this section the discussion related to the "sharp linear feature"). Only very low-resolution SAR data are available at the tips of nearby fluvial valleys: extending the above interpretation to other features is therefore not possible. Nevertheless, this single feature was classified as part of the Fluvial

Subunit 2. The lack of extensive SAR data coverage is currently leaving any interpretation with some degree of uncertainty.

The drainage direction during the last active phase of SW Xanadu's fluvial network seems to have been mainly driven by a northwest-southeast local topographic gradient, yet the strong influence of at least 28 (further direct individuation is limited by data resolution) pre-existing east-west, southwest-northeast and northwest-southeast linear features is recorded in the present-day geomorphology (azimuthal analysis' results shown in Figure 2b, see Section 3.2). The changes in direction of the fluvial valleys along these linear features follow a linear pattern with near-right angle bends, as in a tectonic-controlled rectangular drainage pattern (Howard, 1967; Burr et al., 2009; Burr, Drummond, et al., 2013; Twidale, 2004). Red lines in Figure 4a-b show examples of where, in the investigated area, this effect is most evident. If such features were related to thrust faulting, arcuate morphologies in planar view would be observed, which are not (for a discussion on this topic related to Titan, see Liu, Radebaugh, Harris, Christiansen, & Rupper, 2016; Liu, Radebaugh, Harris, Christiansen, Neish, et al., 2016). Normal faulting in this area would have generated vertical displacements of some extent, which are not observed on the available topographic data. The horizontal displacements noticeable on both SAR and topographic data suggest instead the occurrence of small-scale strike-slip faulting in this part of SW Xanadu (Figure 4 a-b).

In the northern portions of the mapped area (around 2°S; 127°W) three aligned structures have been encountered (Figure 4c). These are already described in literature (Mitri et al., 2010; Radebaugh et al., 2016) and were interpreted in such works as long-wavelength folds formed by compressional tectonics (IAU nomenclature: "Mithrim Montes").

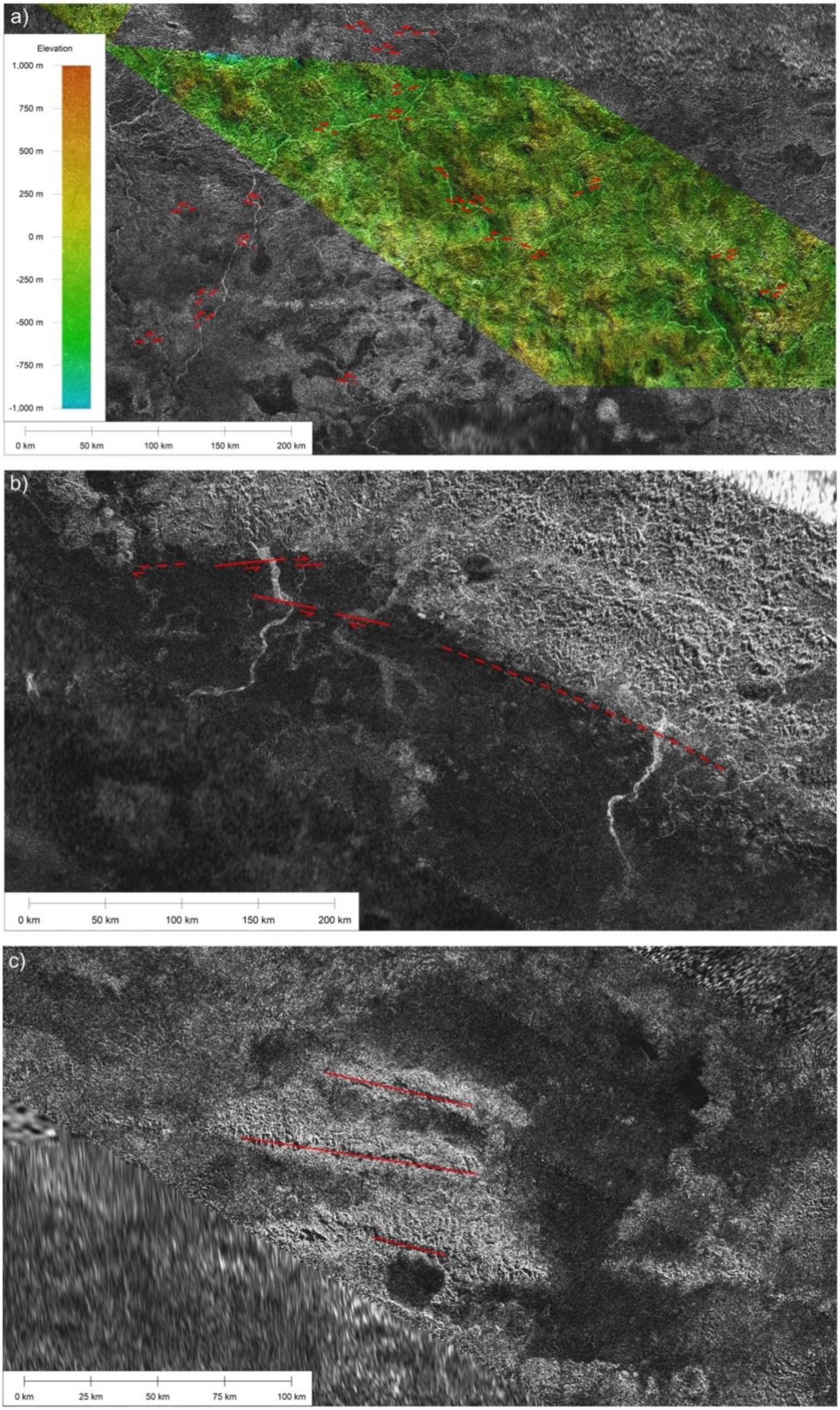
a)
Elevation
1,000 m
750 m
500 m
250 m
0 m
-250 m
-500 m
-750 m
-1,000 m
0 km
50 km
100 km
150 km
200 km
b)
0 km
50 km
100 km
150 km
200 km
c)
0 km
25 km
50 km
75 km
100 km

521

Figure 4. a) Strike-slip faults in central SW Xanadu, shown on a DTM (in overlay visualization) over SAR mosaic. Such faults are marked with red lines; the inferred motion direction is indicated. Their azimuthal analysis' results are shown in Figure 2b. **b)** SAR mosaic displaying the area around the sharp linear feature (20°S; 118°W to 15°S; 128°W, shown as a fault and marked using a red dashed line) described in the text. Other smaller strike-slip faults are shown. **c)** SAR mosaic displaying the area around Mithrim Montes, with their ridges' alignments marked by red lines.
North is up in each panel.

The proposed interpretation of the north-south striking linear feature (centered at 10°S; 110°W; solid red line in Figure 5, henceforth termed Fault 1) is of a normal fault plane extending for ~170 km (knowledge limited by DTM's size). This hypothesis is supported by the local topographic trend and by the nearly constant values of the plane's dip angle (2-6°, Figure 5c-d). Such fault plane is west-dipping (Figure 5c). It is not possible to infer the depths reached by Fault 1 with the available data, but, considering its planar extension of at least ~170 km, it is possible to assume that it constitutes a structure of some relevance, i.e., reaching depths within the first few kilometers of the ice shell, and it is then likely listric.

The two linear features (centered at 9°S; 108°W and 11°S; 108°W, respectively; dashed red lines in Figure 5, henceforth termed Fault 2 and Fault 3), striking roughly NW-SE (dip direction ~200°W) parallel to each other, are interpreted as normal fault planes, both extending for ~150 km. Geomorphic and topographic factors similar to those related to Fault 1 support such hypothesis. These fault planes, however, appear somehow fainter and less continuous on DTM data (Figure 5b-c), which may suggest their older age (considering the deposition of atmospheric precipitates and some degree of erosion through time; Lunine & Lorenz, 2009). Due to the aforementioned observations, to the different orientation in relation to Fault 1 yet similar extensional kinematic and, most importantly, by

considering that they are crosscut by Fault 1 (Figure 5b-c), Fault 2 and 3 are thus interpreted as belonging to a previous tectonic phase.

The sharp linear feature extending from 20°S; 118°W to 15°S; 128°W (Figure 1, Figure 4b) strikes parallel to Fault 2 and 3. Going along-dip on this feature, a distinct change in terrain characteristics is evident (on SAR data, Figure 1a and Figure 4b). Moreover, the local fluvial features show a significant increase in width size crossing it north to south, suggesting the presence of an important topographic drop. Despite the lack of consistent topographic data (no DTMs; local SARTopo data run parallel to it and are therefore of limited use) over its location, the above considerations led to the interpretation of such feature as a normal fault, in agreement with Radebaugh et al. (2011). This fault would have developed throughout the same tectonic phase of Fault 2 and 3, given their parallel strike.

In the western parts of the investigated area, the presence of one or more normal faults is inferred: local topographic highs followed by distinct drops are in fact observed east of the Shangri-La dune field (from ~10°S; 142°W to ~3°S; 138°W, Section 3.2, Figure 1c-d and Figure 3). Such high relief might represent a topographic barrier for the Shangri-La dunes, which stop abruptly at this boundary. However, Barnes et al. (2015) suggested instead that SW Xanadu's rivers could likely be a barrier for the Shangri-La dunes, by analogy with the Namib Desert. Distinct fault planes cannot be directly identified, as the surface is intensely reworked and masked by fluvial activity. Nevertheless, the observed, marked elevation drops are limited to a relatively small area and occur along sharp east-dipping slopes (as described in Section 3.2), suggesting the occurrence of normal faulting. Without the presence of the numerous fluvial features, we would probably observe tectonic structures similar to those previously described to the eastern parts of the investigated area, as the topographical characteristics are analogous (description in Section 3.2).

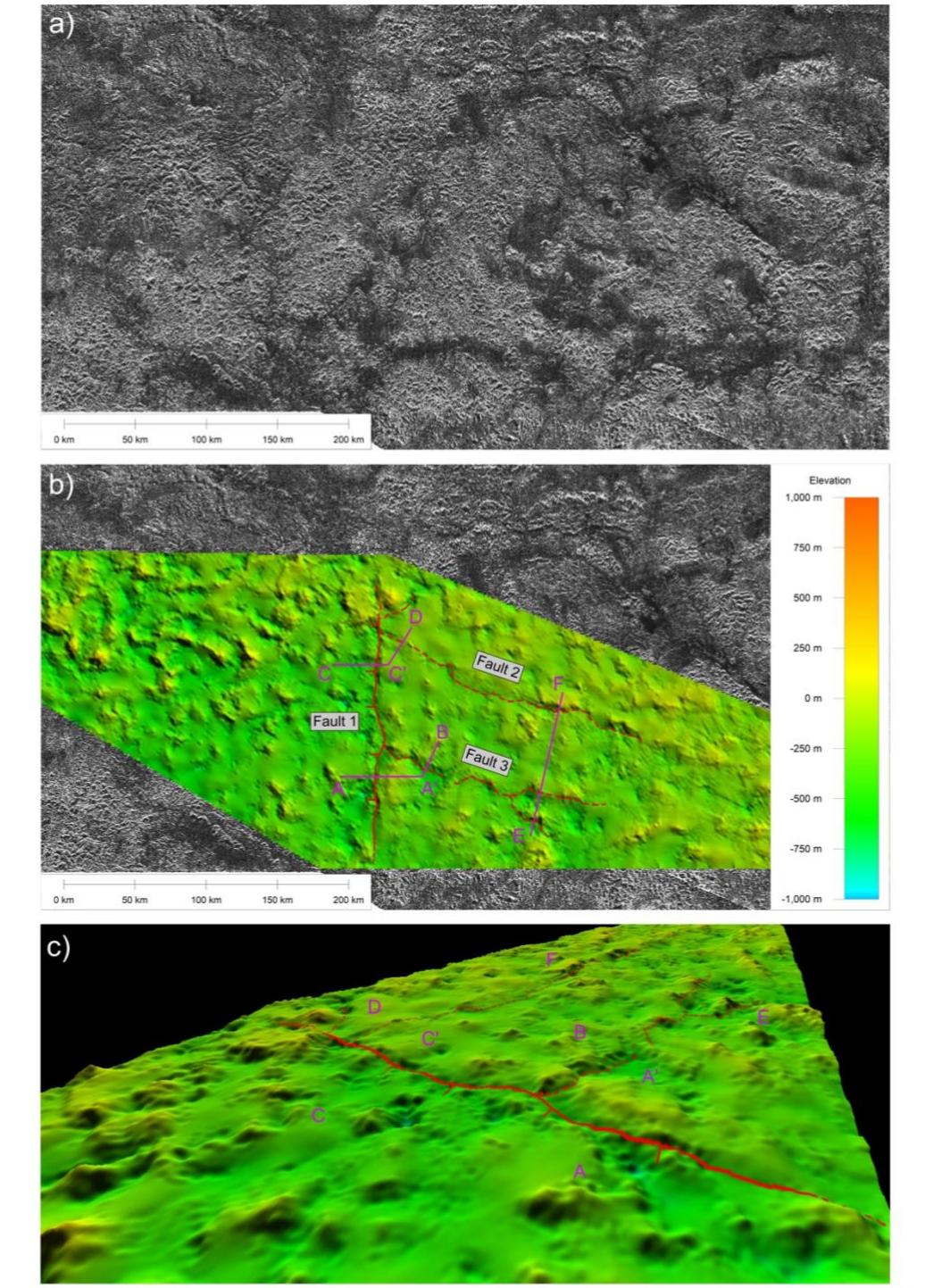
a)
0 km
50 km
100 km
150 km
200 km
b)
Elevation
1,000 m
750 m
500 m
250 m
0 m
-250 m
-500 m
-750 m
-1,000 m
Fault 1
Fault 2
Fault 3
A
A'
B
C
C'
D
E
F
c)
d)
0 m
-250 m
-500 m
10 km
20 km
30 km
40 km
50 km
60 km
70 km
25 km
75 km
100 km

570 **Figure 5. a)** SAR mosaic, displaying the area enclosed by the red dashed polygon in Figure 3. **b)**
571 DTM in 2D visualization overlain on the SAR mosaic shown in panel a. Hill-shading is enabled, with
572 a vertical exaggeration factor of 5. Three distinct fault planes are recognizable: Fault 1 is marked as
573 a solid red line, Fault 2 and 3 as dashed red lines since they look fainter on DTM data, which probably
574 implies their older age, as described in the text. North is up in panels a and b. **c)** DTM in 3D
575 visualization, vertical exaggeration factor of 10. The area and the features shown are the same as in
576 the previous panels; no SAR mosaic in the background. Faults 1, 2 and 3 are marked as in panel b. **d)**
577 Topographic profiles, as traced on the map in previous panels. Fault traces are displayed, with their
578 hypothetical inclinations at increasing depths, as listric faults, which tend to flatten with depth. Solid
579 or dashed red lines correspond to Fault 1 or Fault 2-3, respectively.
580
581
582 **4. Discussion and conclusions**
583 The hypothesis that Titan has experienced some kind of tectonic activity in the past is strongly
584 supported by both observational data (e.g., eroded mountain chains; Liu, Radebaugh, Harris,
585 Christiansen, Neish, et al., 2016; Radebaugh et al., 2007) and modeling (e.g., compression related
586 long-wavelength folds and fold-and-thrust belts, Mitri et al., 2010). Nevertheless, the intense erosion
587 that affected the mountain ranges and the lack of evidences for recent orogenic features suggest that
588 such tectonic activity has probably ceased and might be long-time quiescent (Langhans et al., 2013;
589 Radebaugh et al., 2011).
590 Southwestern Xanadu's characteristics can provide useful insights on Titan's overall tectonic
591 setting. Radebaugh et al. (2011) proposed that in a first tectonic phase, the region underwent crustal
592 thickening via north-south directed regional-scale compression. This phase would have had surface
593 expressions such as east-west oriented parallel mountain ridges (and related valleys) and fold-and-
594 thrust belts. A subsequent extensional event has been invoked to explain present-day Xanadu low
595 elevation, favored by slip along region-bounding faults, resulting in horst-and-graben structures.

Langhans et al. (2013) substantially agreed with the evolutionary model proposed by Radebaugh et al. (2011), yet stressing the important role of rivers as a landscape-shaping factor. They studied in detail SW Xanadu fluvial network's azimuths, ending up in assessing an almost uniform azimuthal distribution. An analysis of the relationship between valley network orientations and the present-day topography (Black et al., 2017), further indicates how Titan's mid-latitude and equatorial regions have been stable since the fluvial networks' imposition.

Our fluvial azimuths' rose diagram results are consistent with those reported by Langhans et al. (2013). Even though we have used a larger data population, we identified a broad distribution of azimuths, yet with a strong maximum roughly aligned east-west (Figure 2a). The outcome of our study is in concordance with previous works as well (Burr et al., 2009; Burr, Drummond, et al., 2013), which analyzed the main branch of the fluvial network in SW Xanadu and reported that the azimuths have a preferential trend along an east-west orientation. The authors proposed that such orientations form a rectangular-type drainage pattern developed under the influence of tectonic control, with tributaries' azimuths that indicate an east-west tectonic fabric. They considered (Burr et al., 2009) that the regional slope was southward at the time of fluvial network's onset, as indicated by the overall network elongation and the fluvial links converging in a southerly direction. Burr, Drummond, et al. (2013) have inferred that the tectonic style responsible for generating such rectangular-type drainage pattern was likely extensional, mainly by analogy with terrestrial examples. They observed that the fluvial network has links oriented in a small number of preferred directions, instead in the case of branching (or dendritic) networks the links' orientations would be primarily controlled by the slope direction. The results of the present analysis are in agreement with the above studies, as the rectangularity of the drainage pattern supports the hypothesis of pre-existing tectonic control on SW Xanadu's fluvial network (Howard, 1967; Twidale, 2004), yet we propose a variant interpretation for the involved tectonic style. As described in Section 3.2.1, in the central parts of the mapped area, characterized by the presence of the fluvial network, we could not find evidences of extensional faults

622 that would have been responsible for generating a rectangular drainage pattern. Instead, we
623 interpreted the observed features as expressions of small-scale strike-slip faulting (Figure 2b and
624 Figure 4a). We have indeed encountered evidences of extensional faulting, although in other parts of
625 SW Xanadu, as it is discussed below.
626
627 Xanadu's horst-and graben model (Radebaugh et al., 2011) is considered to generally explain the
628 large-scale evolution of this region. In the smaller-scale area we have analyzed, southwestern Xanadu,
629 the local morphotectonic evidences could possibly be traced back to the proposed sequence of events
630 (compression and subsequent extension). On the other hand, the extensive application of qualitative
631 analysis on previously unavailable DTMs, has allowed us to interpret such morphotectonic features
632 as originating from a more specific sequence of events characterizing SW Xanadu's evolution:
633
634 1) Ancient extensional phase along NW-SE faults.
635 Its expressions are:
636 - Two NW-SE striking normal faults centered at 9°S; 108°W and 11°S; 108°W, named
637 Fault 2 and Fault 3, respectively (Figure 5);
638
639 - One NW-SE striking normal fault extending from 20°S; 118°W to 15°S; 128°W (Figure
640 4b), in agreement with the interpretation given by Radebaugh et al. (2011).
641
642 Each of these structures are parallel to each other and have a dip direction of ~200°W (see Section
643 3.2.1 for the interpretation as normal faults). This phase's surficial expressions have probably been
644 wiped out, for the most part, by the subsequent tectonic phase and the intense fluvial activity. Indeed,
645 we could identify its expressions mainly to the easternmost parts of SW Xanadu, where there are very
646 few fluvial features compared to its central and western parts (Figure 1a-b).
647

2) More recent tectonic phase driven by large-scale transcurrent faulting (transtensional phase). Its expressions are:

- One north-south striking normal fault centered at 10°S; 110°W, named Fault 1 (Figure 5), crosscutting both Fault 2 and Fault 3, which confirms its younger age;

- One or more north-south striking normal faults (inferred), located in an area around ~10°S; 142°W to ~3°S; 138°W (Figure 3). Distinct fault planes cannot be directly identified, as the surface is intensely reworked and masked by fluvial activity. Nevertheless, the observed, marked elevation drops are limited to a relatively small area and occur along sharp east-dipping slopes, suggesting the occurrence of normal faulting;

- Three aligned structures (Mithrim Montes) located around 2°S; 127°W (Figure 4c). These are interpreted in literature (Mitri et al., 2010; Radebaugh et al., 2016) as long-wavelength folds formed by compressional tectonics. In absence of additional topographic data (DTMs) on the relevant location, we reckon these structures as being compression related;

- Several E-W, NW-SE and SW-NE small-scale strike-slip faults distributed all over central SW Xanadu (Figure 4a). The local fluvial network has imposed on these pre-existing features, as evidenced by several abrupt changes in the fluvial valleys' directions, resulting in a rectangular-type drainage pattern.

All the surficial expressions of the second tectonic phase are shown in a conceptual model in Figure 6.

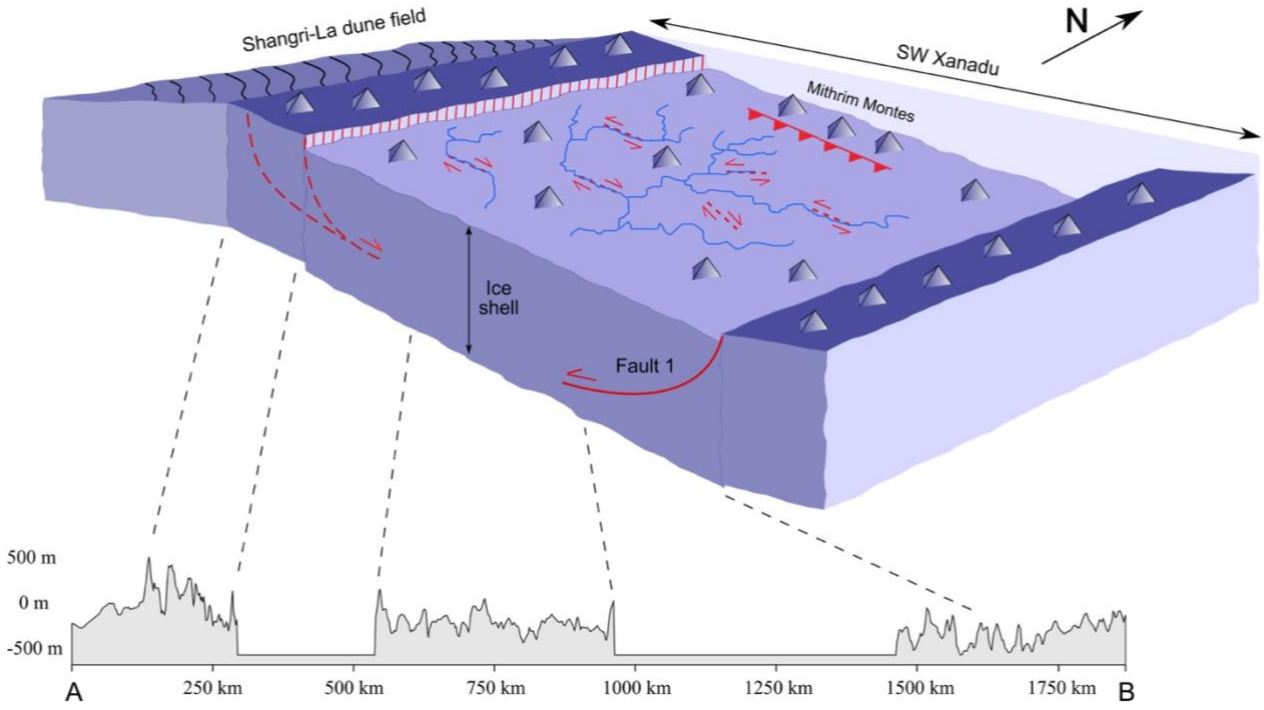

Figure 6. Top) Sketched representation of the tectonic setting at southwestern Xanadu. To the west, SW Xanadu is bordered by the Shangri-La dune field. Close to the transition between these two regions, we inferred the presence of one or more normal faults (which are therefore hypothetical and are marked here as dashed red lines). To the north, some compressional structures were identified, which were already known in literature as "Mithrim Montes". To the east, a normal fault was identified (Fault 1, marked as a solid red line). Overall, this tectonic setting results in a horst-and-graben or half-graben structure. Central SW Xanadu represents the graben, characterized by a fluvial network imposing on pre-existing linear features, which are interpreted as strike-slip faults.

Bottom) Corresponding topographic profile based on data of three different DTMs (vertical error range: ± 100 m), with its location on Titan's SAR mosaic as shown in Figure 3. The sudden breaks of the profile are due to non-available DTM data in the corresponding locations. SW Xanadu's westernmost part is separated from the Shangri-La dune field to the west by elevation drops, along east-dipping slopes, followed by topographic highs. These marked elevation drops are interpreted as being due to normal faulting, which is not directly observed but appears evident from topographic

689 profiles (see also Figure 3). The high relief in the western part of SW Xanadu might as well represent
690 a topographic barrier for the Shangri-La dunes, which stop abruptly at this boundary. To the east of
691 central SW Xanadu, the identification of a continuous, west-dipping plane, characterized by a nearly
692 constant dip angle (Figure 5) led to interpret it as a large-scale tectonic structure, specifically a normal
693 fault (termed Fault 1).
694
695
696 The theoretical structural model proposed (Figure 7) combines all the surficial expressions of the
697 aforementioned second tectonic phase (considered as being the last active one in this area). Generally,
698 in a transtensional setting the master fault is a large-scale transcurrent structure (see Section 1), whose
699 main stresses can be divided into their compressional and extensional components (Fossen et al.,
700 1994; Petit, 1987). In the case of SW Xanadu, the extensional component should have been more
701 intense as it generated large-scale and well-developed structures compared to those related to
702 compressional stresses. Thus, such stress field generated a tectonic depression in its central portions,
703 specifically termed pull-apart basin (Mann et al., 1983). The smaller-scale strike-slip faults
704 characterizing central SW Xanadu would have been formed in this setting as well, as synthetic and
705 antithetic Riedel structures to the transcurrent master fault (Fossen et al., 1994; Petit, 1987). It must
706 be noticed that we did not directly observe said master fault, as it should be a regional-scale structure
707 located outside of the mapped area, yet its direction (roughly SW-NE) was inferred by analyzing the
708 angular relationships of SW Xanadu's aforementioned structures, as identified through
709 geomorphological and topographical analysis. We could not locate one of the compressional
710 structures hypothesized in the structural model, which predicts symmetrical thrust faulting on both
711 sides of the strain ellipse. Evidences of thrust faulting were in fact identified just to the north of the
712 mapped area (Mithrim Montes; around 2°S; 127°W) while not to the south. Anyhow, this is probably
713 due to the absence of topographic data and lack of SAR images in the southern parts of the mapped
714 area.

Such transtensional structural model is in agreement with Titan's global radial contraction through volume decrease predicted in Mitri et al. (2010), considering SW Xanadu's master transcurrent fault as being related to other potential structures with similar kinematic around equatorial latitudes: if the ice shell has lateral thickness variations (thinner in the polar regions), then the radial contraction of Titan, when coupled with rotational spin-up, generates a global N-S directed stress field (Cook-Hallett et al., 2015; Melosh, 1977; Mitri et al., 2010). In this setting, large-scale NE-SW or NW-SE transcurrent faulting would be likely to occur, within 30° of the equator (Cook-Hallett et al., 2015).

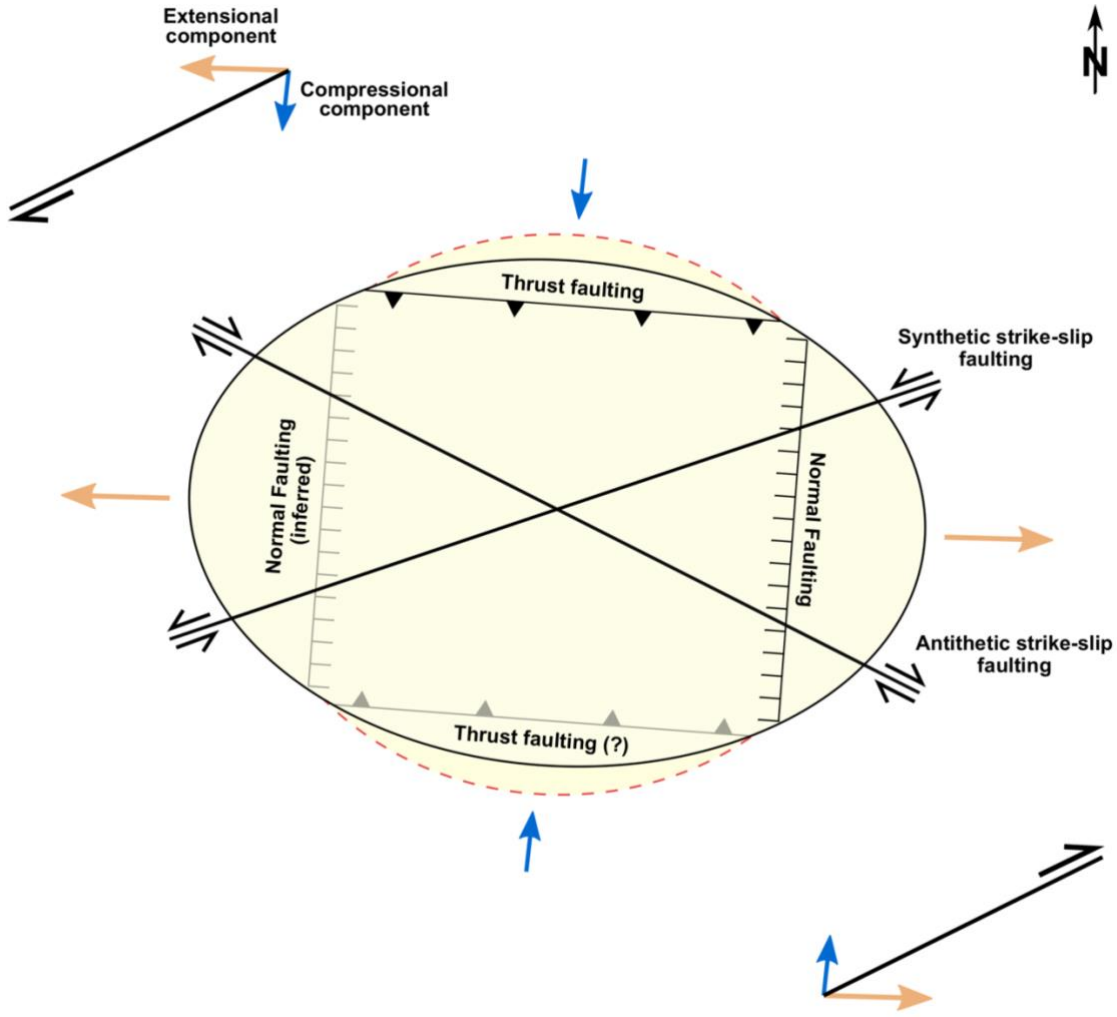

Figure 7. SW Xanadu's theoretical structural model at a regional scale. Strain ellipses are displayed in light yellow. Riedel structures, formed following transtensional kinematic criteria driven by large-scale transcurrent faulting, are shown in black. All of SW Xanadu's features described in the text are located within the strain ellipses.

We conclude that central SW Xanadu is a depression formed by transtensional tectonic activity, i.e., it is a pull-apart basin, bordered to the west and east by large-scale normal faulting and to the north and (probably) south by thrust faulting of lesser relevance. Such pull-apart basin is characterized by strike-slip faulting within it, on which a fluvial network has subsequently imposed. This model may explain how SW Xanadu has lower elevations compared to its surroundings, while still being a topographically rugged region.

Acknowledgments

We gratefully acknowledge the insightful comments of Elizabeth P. Turtle, Jani Radebaugh and an anonymous reviewer. PM was supported by Latium Region's Study and Knowledge Promotion (DiSCo) Programme 2018-19, European Social Fund 2014-20. SAR data and related by-products used in this manuscript can be accessed from the PDS Cartography and Imaging Science Node (https://pds-imaging.jpl.nasa.gov/volumes/radar.html). Data of the geomorphological map (Figure 1b) and of the rose diagrams (Figure 2) are available on TRR 170-DB https://planetary-data-portal.org/privateurl.xhtml?token=1d63e6b7-118a-473e-a86f-46adf4810b9a (Matteoni et al., 2020).

References

Aharonson, O., Hayes, A. G., Hayne, P. O., Lopes, R. M., Lucas, A., & Perron, J. T. (2013). *Titan*. (I. Muller-Wodarg, C. A. Griffith, E. Lellouch, & T. E. Cravens, Eds.), *Titan: Interior, Surface, Atmosphere, and Space Environment*. Cambridge: Cambridge University Press. https://doi.org/10.1017/CBO9780511667398

752 Arthur David Howard. (1967). Drainage Analysis in Geologic Interpretation: A Summation. *AAPG*
753 *Bulletin*, *51*, 2246–2259. https://doi.org/10.1306/5D25C26D-16C1-11D7-8645000102C1865D
754 Barnes, J. W., Brown, R. H., Soderblom, L., Buratti, B. J., Sotin, C., Rodriguez, S., et al. (2007).
755 Global-scale surface spectral variations on Titan seen from Cassini/VIMS. *Icarus*, *186*(1), 242–
756 258. https://doi.org/10.1016/j.icarus.2006.08.021
757 Barnes, J. W., Radebaugh, J., Brown, R. H., Wall, S., Soderblom, L., Lunine, J., et al. (2007). Near-
758 infrared spectral mapping of Titan's mountains and channels. *Journal of Geophysical Research*
759 *E: Planets*, *112*(11). https://doi.org/10.1029/2007JE002932
760 Barnes, J. W., Brown, R. H., Soderblom, L., Sotin, C., Le Mouèlic, S., Rodriguez, S., et al. (2008).
761 Spectroscopy, morphometry, and photoclinometry of Titan's dunefields from Cassini/VIMS.
762 *Icarus*, *195*(1), 400–414. https://doi.org/10.1016/j.icarus.2007.12.006
763 Barnes, J. W., Lorenz, R. D., Radebaugh, J., Hayes, A. G., Arnold, K., & Chandler, C. (2015).
764 Production and global transport of Titan's sand particles. *Planetary Science*, *4*(1), 1.
765 https://doi.org/10.1186/s13535-015-0004-y
766 Birch, S. P. D., Hayes, A. G., Howard, A. D., Moore, J. M., & Radebaugh, J. (2016). Alluvial Fan
767 Morphology, distribution and formation on Titan. *Icarus*, *270*, 238–247.
768 https://doi.org/10.1016/j.icarus.2016.02.013
769 Birch, S. P. D., Hayes, A. G., Dietrich, W. E., Howard, A. D., Bristow, C. S., Malaska, M. J., et al.
770 (2017). Geomorphologic mapping of titan's polar terrains: Constraining surface processes and
771 landscape evolution. *Icarus*, *282*, 214–236. https://doi.org/10.1016/j.icarus.2016.08.003
772 Birch, S. P. D., Hayes, A. G., Corlies, P., Stofan, E. R., Hofgartner, J. D., Lopes, R. M. C., et al.
773 (2018). Morphological evidence that Titan's southern hemisphere basins are paleoseas. *Icarus*,
774 *310*, 140–148. https://doi.org/10.1016/j.icarus.2017.12.016
775 Black, B. A., Perron, J. T., Burr, D. M., & Drummond, S. A. (2012). Estimating erosional exhumation
776 on Titan from drainage network morphology. *Journal of Geophysical Research: Planets*,
777 *117*(E8), n/a-n/a. https://doi.org/10.1029/2012JE004085

778 Black, B. A., Perron, J. T., Hemingway, D., Bailey, E., Nimmo, F., & Zebker, H. (2017). Global
779 drainage patterns and the origins of topographic relief on Earth, Mars, and Titan. *Science*,
780 *356*(6339), 727–731. https://doi.org/10.1126/science.aag0171
781 Bonnefoy, L. E., Hayes, A. G., Hayne, P. O., Malaska, M. J., Le Gall, A., Solomonidou, A., & Lucas,
782 A. (2016). Compositional and spatial variations in Titan dune and interdune regions from Cassini
783 VIMS and RADAR. *Icarus*, *270*, 222–237. https://doi.org/10.1016/j.icarus.2015.09.014
784 Bottke, W. F., & Norman, M. D. (2017). The Late Heavy Bombardment. *Annual Review of Earth and*
785 *Planetary Sciences*, *45*(1), 619–647. https://doi.org/10.1146/annurev-earth-063016-020131
786 Brown, R. H., Baines, K. H., Bellucci, G., Bibring, J.-P., Buratti, B. J., Capaccioni, F., et al. (2004).
787 The Cassini Visual And Infrared Mapping Spectrometer (Vims) Investigation. *Space Science*
788 *Reviews*, *115*(1–4), 111–168. https://doi.org/10.1007/s11214-004-1453-x
789 Brown, Robert H., Barnes, J. W., & Melosh, H. J. (2011). On Titan's Xanadu region. *Icarus*, *214*(2),
790 556–560. https://doi.org/10.1016/j.icarus.2011.03.018
791 Burr, D. M., Jacobsen, R. E., Roth, D. L., Phillips, C. B., Mitchell, K. L., & Viola, D. (2009). Fluvial
792 network analysis on Titan: Evidence for subsurface structures and west-to-east wind flow,
793 southwestern Xanadu. *Geophysical Research Letters*, *36*(22), L22203.
794 https://doi.org/10.1029/2009GL040909
795 Burr, D. M., Taylor Perron, J., Lamb, M. P., Irwin, R. P., Collins, G. C., Howard, A. D., et al. (2013).
796 Fluvial features on Titan: Insights from morphology and modeling. *Geological Society of*
797 *America Bulletin*, *125*(3–4), 299–321. https://doi.org/10.1130/B30612.1
798 Burr, D. M., Drummond, S. A., Cartwright, R., Black, B. A., & Perron, J. T. (2013). Morphology of
799 fluvial networks on Titan: Evidence for structural control. *Icarus*, *226*(1), 742–759.
800 https://doi.org/10.1016/j.icarus.2013.06.016
801 Callegari, M., Casarano, D., Mastrogiuseppe, M., Poggiali, V., & Notarnicola, C. (2014). Dune
802 Height Estimation on Titan Exploiting Pairs of Synthetic Aperture Radar Images With Different
803 Observation Angles. *IEEE Journal of Selected Topics in Applied Earth Observations and*

804 *Remote Sensing*, *8*(3), 1–12. https://doi.org/10.1109/JSTARS.2014.2352037
805 Cartwright, R., Clayton, J. A., & Kirk, R. L. (2011). Channel morphometry, sediment transport, and
806 implications for tectonic activity and surficial ages of Titan basins. *Icarus*, *214*(2), 561–570.
807 https://doi.org/10.1016/j.icarus.2011.03.011
808 Cartwright, R. J., & Burr, D. M. (2017). Using Synthetic Aperture Radar data of terrestrial analogs
809 to test alluvial fan formation mechanisms on Titan. *Icarus*, *284*, 183–205.
810 https://doi.org/10.1016/j.icarus.2016.11.013
811 Cook-Hallett, C., Barnes, J. W., Kattenhorn, S. A., Hurford, T., Radebaugh, J., Stiles, B., & Beuthe,
812 M. (2015). Global contraction/expansion and polar lithospheric thinning on Titan from patterns
813 of tectonism. *Journal of Geophysical Research: Planets*, *120*(6), 1220–1236.
814 https://doi.org/10.1002/2014JE004645
815 Corlies, P., Hayes, A. G., Birch, S. P. D., Lorenz, R., Stiles, B. W., Kirk, R., et al. (2017). Titan's
816 Topography and Shape at the End of the Cassini Mission. *Geophysical Research Letters*, *44*(23),
817 11,754-11,761. https://doi.org/10.1002/2017GL075518
818 Coustenis, A., Tokano, T., Burger, M. H., Cassidy, T. A., Lopes, R. M., Lorenz, R. D., et al. (2010).
819 Atmospheric/exospheric characteristics of icy satellites. *Space Science Reviews*, *153*(1–4), 155–
820 184. https://doi.org/10.1007/s11214-009-9615-5
821 Coustenis, Athena. (2005). Formation and evolution of Titan's atmosphere. *Space Science Reviews*,
822 *116*(1–2), 171–184. https://doi.org/10.1007/s11214-005-1954-2
823 Dalton, J. B., Cruikshank, D. P., Stephan, K., McCord, T. B., Coustenis, A., Carlson, R. W., &
824 Coradini, A. (2010). *Chemical composition of icy satellite surfaces*. *Space Science Reviews* (Vol.
825 153). https://doi.org/10.1007/s11214-010-9665-8
826 Elachi, C., Allison, M. D., Borgarelli, L., Encrenaz, P., Im, E., Janssen, M. A., et al. (2004). Radar:
827 The Cassini Titan Radar Mapper. *Space Science Reviews*, *115*(1–4), 71–110.
828 https://doi.org/10.1007/s11214-004-1438-9
829 Elachi, C., Wall, S., Janssen, M., Stofan, E., Lopes, R., Kirk, R., et al. (2006). Titan Radar Mapper

observations from Cassini's T3 fly-by. *Nature*, *441*(7094), 709–713. https://doi.org/10.1038/nature04786

Ford, J. P., Weitz, J. J. P. C. M., Farr, T. G., Senske, D. A., Stofan, E. R., Michaels, G., & Parker, T. J. (1993). *Guide to Magellan Image Interpretation*. *Jet Propulsion Laboratory, Cap. Radar Interactions With Geologic Surfaces*. Retrieved from http://web.archive.org/web/19990420173536/http://pds.jpl.nasa.gov/mgddf/guide.htm

Fossen, H., Tikoff, B., & Teyssier, C. (1994). Strain modeling of transpressional and transtensional deformation. *Norsk Geologisk Tidsskrift*, *74*(3), 134–145.

Le Gall, A., Janssen, M. A., Paillou, P., Lorenz, R. D., & Wall, S. D. (2010). Radar-bright channels on Titan. *Icarus*, *207*(2), 948–958. https://doi.org/10.1016/j.icarus.2009.12.027

Le Gall, A., Janssen, M. A., Wye, L. C., Hayes, A. G., Radebaugh, J., Savage, C., et al. (2011). Cassini SAR, radiometry, scatterometry and altimetry observations of Titan's dune fields. *Icarus*, *213*(2), 608–624. https://doi.org/10.1016/j.icarus.2011.03.026

Gürbüz, A. (2010). Geometric characteristics of pull-apart basins. *Lithosphere*, *2*(3), 199–206. https://doi.org/10.1130/L36.1

Hayes, A., Aharonson, O., Callahan, P., Elachi, C., Gim, Y., Kirk, R., et al. (2008). Hydrocarbon lakes on Titan: Distribution and interaction with a porous regolith. *Geophysical Research Letters*, *35*(9), L09204. https://doi.org/10.1029/2008GL033409

Hayes, A. G. (2016). The Lakes and Seas of Titan. *Annual Review of Earth and Planetary Sciences*, *44*(1), 57–83. https://doi.org/10.1146/annurev-earth-060115-012247

Hayes, A. G., Lorenz, R. D., & Lunine, J. I. (2018). A post-Cassini view of Titan's methane-based hydrologic cycle. *Nature Geoscience*, *11*(5), 306–313. https://doi.org/10.1038/s41561-018-0103-y

Hedgepeth, J. E., Neish, C. D., Turtle, E. P., Stiles, B. W., Kirk, R., & Lorenz, R. D. (2020). Titan's impact crater population after Cassini. *Icarus*, 113664. https://doi.org/10.1016/j.icarus.2020.113664

856 Howard, A. D. (2009). How to make a meandering river. *Proceedings of the National Academy of*
857 *Sciences*, *106*(41), 17245–17246. https://doi.org/10.1073/pnas.0910005106
858 Iess, L., Jacobson, R. A., Ducci, M., Stevenson, D. J., Lunine, J. I., Armstrong, J. W., et al. (2012).
859 The tides of Titan. *Science*, *337*(6093), 457–459. https://doi.org/10.1126/science.1219631
860 Janssen, M. A., Lorenz, R. D., West, R., Paganelli, F., Lopes, R. M., Kirk, R. L., et al. (2009). Titan's
861 surface at 2.2-cm wavelength imaged by the Cassini RADAR radiometer: Calibration and first
862 results. *Icarus*, *200*(1), 222–239. https://doi.org/10.1016/j.icarus.2008.10.017
863 Janssen, M. A., Le Gall, A., & Wye, L. C. (2011). Anomalous radar backscatter from Titan's surface?
864 *Icarus*, *212*(1), 321–328. https://doi.org/10.1016/j.icarus.2010.11.026
865 Janssen, M. A., Le Gall, A., Lopes, R. M., Lorenz, R. D., Malaska, M. J., Hayes, A. G., et al. (2016).
866 Titan's surface at 2.18-cm wavelength imaged by the Cassini RADAR radiometer: Results and
867 interpretations through the first ten years of observation. *Icarus*, *270*, 443–459.
868 https://doi.org/10.1016/j.icarus.2015.09.027
869 Jaumann, R., Brown, R. H., Stephan, K., Barnes, J. W., Soderblom, L. A., Sotin, C., et al. (2008).
870 Fluvial erosion and post-erosional processes on Titan. *Icarus*, *197*(2), 526–538.
871 https://doi.org/10.1016/j.icarus.2008.06.002
872 Jay Melosh, H. (1977). Global tectonics of a despun planet. *Icarus*, *31*(2), 221–243.
873 https://doi.org/10.1016/0019-1035(77)90035-5
874 Kim, J., Wan, W., & Kim, Y. (2016). Reconstruction of Titan Topography Using CASSINI Radar
875 Images And Generic Stereo Processor. In *47th Lunar and Planetary Science Conference* (Vol.
876 743, p. 1411).
877 Kirk, R. L., & Howington-Kraus, E. (2008). Radargrammetry on three planets (pp. 973–980).
878 Kirk, R. L., Howington-Kraus, E., Stiles, B. W., & Hensley, S. (2008). Digital Topographic Models
879 of Titan Produced by Radar Stereogrammetry with a Rigorous Sensor Model. In *Lunar and*
880 *Planetary Science XXXIX* (pp. 19–20).
881 Kirk, R. L., Howington-Kraus, E., Redding, B., Callahan, P. S., Hayes, a. G., Le Gall, A., et al. (2012).

882 Topographic Mapping of Titan: Latest Results. In *Lunar and Planetary Science Conference*
883 (Vol. 43, p. 2759). Retrieved from http://adsabs.harvard.edu/abs/2012LPI....43.2759K
884 Langhans, M., Lunine, J. I., & Mitri, G. (2013). Titan's Xanadu region: Geomorphology and
885 formation scenario. *Icarus*, *223*(2), 796–803. https://doi.org/10.1016/j.icarus.2013.01.016
886 Langhans, M. H., Jaumann, R., Stephan, K., Brown, R. H., Buratti, B. J., Clark, R. N., et al. (2012).
887 Titan's fluvial valleys: Morphology, distribution, and spectral properties. *Planetary and Space*
888 *Science*, *60*(1), 34–51. https://doi.org/10.1016/j.pss.2011.01.020
889 Liu, Z. Y.-C., Radebaugh, J., Harris, R. A., Christiansen, E. H., & Rupper, S. (2016). Role of fluids
890 in the tectonic evolution of Titan. *Icarus*, *270*, 2–13.
891 https://doi.org/10.1016/j.icarus.2016.02.016
892 Liu, Z. Y.-C., Radebaugh, J., Harris, R. A., Christiansen, E. H., Neish, C. D., Kirk, R. L., & Lorenz,
893 R. D. (2016). The tectonics of Titan: Global structural mapping from Cassini RADAR. *Icarus*,
894 *270*, 14–29. https://doi.org/10.1016/j.icarus.2015.11.021
895 Lopes, R. M. C., Stofan, E. R., Peckyno, R., Radebaugh, J., Mitchell, K. L., Mitri, G., et al. (2010).
896 Distribution and interplay of geologic processes on Titan from Cassini radar data. *Icarus*, *205*(2),
897 540–558. https://doi.org/10.1016/j.icarus.2009.08.010
898 Lopes, R. M. C., Malaska, M. J., Solomonidou, A., Le Gall, A., Janssen, M. A., Neish, C. D., et al.
899 (2016). Nature, distribution, and origin of Titan's Undifferentiated Plains. *Icarus*, *270*(July
900 2013), 162–182. https://doi.org/10.1016/j.icarus.2015.11.034
901 Lopes, R. M. C., Wall, S. D., Elachi, C., Birch, S. P. D., Corlies, P., Coustenis, A., et al. (2019). Titan
902 as Revealed by the Cassini Radar. *Space Science Reviews*, *215*(4), 33.
903 https://doi.org/10.1007/s11214-019-0598-6
904 Lopes, R. M. C., Malaska, M. J., Schoenfeld, A. M., Solomonidou, A., Birch, S. P. D., Florence, M.,
905 et al. (2020). A global geomorphologic map of Saturn's moon Titan. *Nature Astronomy*, *4*(3),
906 228–233. https://doi.org/10.1038/s41550-019-0917-6
907 Lorenz, R. D. (2000). The Weather on Titan. *Science*, *290*(5491), 467–468.

908 https://doi.org/10.1126/science.290.5491.467
909 Lorenz, R. D., Wall, S., Radebaugh, J., Boubin, G., Reffet, E., Janssen, M., et al. (2006). The Sand
910 Seas of Titan: Cassini RADAR Observations of Longitudinal Dunes. *Science*, *312*(5774), 724–
911 727. https://doi.org/10.1126/science.1123257
912 Lorenz, Ralph D., Lopes, R. M., Paganelli, F., Lunine, J. I., Kirk, R. L., Mitchell, K. L., et al. (2008).
913 Fluvial channels on Titan: Initial Cassini RADAR observations. *Planetary and Space Science*,
914 *56*(8), 1132–1144. https://doi.org/10.1016/j.pss.2008.02.009
915 Lorenz, Ralph D., Stiles, B. W., Aharonson, O., Lucas, A., Hayes, A. G., Kirk, R. L., et al. (2013). A
916 global topographic map of Titan. *Icarus*, *225*(1), 367–377.
917 https://doi.org/10.1016/j.icarus.2013.04.002
918 Lunine, J. I. (2017). Ocean worlds exploration. *Acta Astronautica*, *131*(November 2016), 123–130.
919 https://doi.org/10.1016/j.actaastro.2016.11.017
920 Lunine, J. I., & Lorenz, R. D. (2009). Rivers, Lakes, Dunes, and Rain: Crustal Processes in Titan's
921 Methane Cycle. *Annual Review of Earth and Planetary Sciences*, *37*(1), 299–320.
922 https://doi.org/10.1146/annurev.earth.031208.100142
923 Malaska, M. J., Lopes, R. M. C., Williams, D. A., Neish, C. D., Solomonidou, A., Soderblom, J. M.,
924 et al. (2016). Geomorphological map of the Afekan Crater region, Titan: Terrain relationships
925 in the equatorial and mid-latitude regions. *Icarus*, *270*, 130–161.
926 https://doi.org/10.1016/j.icarus.2016.02.021
927 Malaska, M. J., Lopes, R. M., Hayes, A. G., Radebaugh, J., Lorenz, R. D., & Turtle, E. P. (2016).
928 Material transport map of Titan: The fate of dunes. *Icarus*, *270*, 183–196.
929 https://doi.org/10.1016/j.icarus.2015.09.029
930 Malaska, M. J., Radebaugh, J., Lopes, R. M. C., Mitchell, K. L., Verlander, T., Schoenfeld, A. M., et
931 al. (2020). Labyrinth terrain on Titan. *Icarus*, (June 2019), 113764.
932 https://doi.org/10.1016/j.icarus.2020.113764
933 Mann, P., Hempton, M. R., Burke, K., & Bradley, D. C. (1983). Development of Pull-Apart Basins.

The Journal of Geology, *91*(5), 529–554.

Mastrogiuseppe, M., Poggiali, V., Seu, R., Martufi, R., & Notarnicola, C. (2014). Titan dune heights retrieval by using Cassini Radar Altimeter. *Icarus*, *230*, 191–197. https://doi.org/10.1016/j.icarus.2013.09.028

Mastrogiuseppe, M., Poggiali, V., Hayes, A. G., Lunine, J. I., Seu, R., Di Achille, G., & Lorenz, R. D. (2018). Cassini radar observation of Punga Mare and environs: Bathymetry and composition. *Earth and Planetary Science Letters*, *496*, 89–95. https://doi.org/10.1016/j.epsl.2018.05.033

Mastrogiuseppe, M., Poggiali, V., Hayes, A. G., Lunine, J. I., Seu, R., Mitri, G., & Lorenz, R. D. (2019). Deep and methane-rich lakes on Titan. *Nature Astronomy*, *3*(535–542). https://doi.org/10.1038/s41550-019-0714-2

Matteoni, P., Mitri, G., Poggiali, V., & Mastrogiuseppe, M. (2020). Replication Data for: Geomorphological analysis of the southwestern margin of Xanadu, Titan: Insights on tectonics. TRR 170-DB. https://doi.org/doi/10.5072/FK2/LKCNM8

Maue, A., & Burr, D. (2018). Updating the Global Map of Titan Fluvial Features and Investigating, *2018*(2066), 7–8.

Mitri, G., Showman, A. P., Lunine, J. I., & Lorenz, R. D. (2007). Hydrocarbon lakes on Titan. *Icarus*, *186*(2), 385–394. https://doi.org/10.1016/j.icarus.2006.09.004

Mitri, G., Bland, M. T., Showman, A. P., Radebaugh, J., Stiles, B., Lopes, R. M. C., et al. (2010). Mountains on Titan: Modeling and observations. *Journal of Geophysical Research E: Planets*, *115*(10), 1–15. https://doi.org/10.1029/2010JE003592

Mitri, G., Meriggiola, R., Hayes, A., Lefevre, A., Tobie, G., Genova, A., et al. (2014). Shape, topography, gravity anomalies and tidal deformation of Titan. *Icarus*, *236*, 169–177. https://doi.org/10.1016/j.icarus.2014.03.018

Mitri, G., Lunine, J. I., Mastrogiuseppe, M., & Poggiali, V. (2019). Possible explosion crater origin of small lake basins with raised rims on Titan. *Nature Geoscience*, *12*(791–796). https://doi.org/10.1038/s41561-019-0429-0

960 Moore, J. M., & Pappalardo, R. T. (2011). Titan: An exogenic world? *Icarus*, *212*(2), 790–806.
961 https://doi.org/10.1016/j.icarus.2011.01.019
962 Moore, J. M., Howard, A. D., & Morgan, A. M. (2014). The landscape of Titan as witness to its
963 climate evolution. *Journal of Geophysical Research: Planets*, *119*(9), 2060–2077.
964 https://doi.org/10.1002/2014JE004608
965 Neish, C. D., & Lorenz, R. D. (2012). Titan's global crater population: A new assessment. *Planetary*
966 *and Space Science*, *60*(1), 26–33. https://doi.org/10.1016/j.pss.2011.02.016
967 Neish, C. D., Molaro, J. L., Lora, J. M., Howard, A. D., Kirk, R. L., Schenk, P., et al. (2016). Fluvial
968 erosion as a mechanism for crater modification on Titan. *Icarus*, *270*, 114–129.
969 https://doi.org/10.1016/j.icarus.2015.07.022
970 Neish, C.D., & Lorenz, R. D. (2014). Elevation distribution of Titan's craters suggests extensive
971 wetlands. *Icarus*, *228*, 27–34. https://doi.org/10.1016/j.icarus.2013.09.024
972 Neish, Catherine D., Lorenz, R. D., Kirk, R. L., & Wye, L. C. (2010). Radarclinometry of the sand
973 seas of Africa's Namibia and Saturn's moon Titan. *Icarus*, *208*(1), 385–394.
974 https://doi.org/10.1016/j.icarus.2010.01.023
975 Nimmo, F. (2018). Icy satellites: Interior structure, dynamics and evolution. In *Oxford Research*
976 *Encyclopedia of Planetary Sciences*. Retrieved from
977 https://websites.pmc.ucsc.edu/~fnimmo/website/Oxford_article_revised.pdf
978 Perron, J. T., Lamb, M. P., Koven, C. D., Fung, I. Y., Yager, E., & Ádámkovics, M. (2006). Valley
979 formation and methane precipitation rates on Titan. *Journal of Geophysical Research*, *111*(E11),
980 E11001. https://doi.org/10.1029/2005JE002602
981 Petit, J. P. (1987). Criteria for the sense of movement on fault surfaces in brittle rocks. *Journal of*
982 *Structural Geology*, *9*(5–6), 597–608. https://doi.org/10.1016/0191-8141(87)90145-3
983 Poggiali, V., Mastrogiuseppe, M., Birch, S. P. D., Lorenz, R., Seu, R., Grima, C., et al. (2016). Liquid-
984 filled canyons on Titan. *Geophysical Research Letters*, *43*(15), 7887–7894.
985 https://doi.org/10.1002/2016gl069679

Porco, C. C., West, R. A., Squyres, S., Mcewen, A., Thomas, P., Murray, C. D., et al. (2004). Cassini Imaging Science: Instrument Characteristics And Anticipated Scientific Investigations At Saturn. *Space Science Reviews*, *115*(1–4), 363–497. https://doi.org/10.1007/s11214-004-1456-7

Porco, C. C., Baker, E., Barbara, J., Beurle, K., Brahic, A., Burns, J. A., et al. (2005). Imaging of Titan from the Cassini spacecraft. *Nature*, *434*(7030), 159–168. https://doi.org/10.1038/nature03436

Radebaugh, J., Lorenz, R. D., Lunine, J. I., Wall, S. D., Boubin, G., Reffet, E., et al. (2008). Dunes on Titan observed by Cassini Radar. *Icarus*, *194*(2), 690–703. https://doi.org/10.1016/j.icarus.2007.10.015

Radebaugh, J., Lorenz, R. D., Wall, S. D., Kirk, R. L., Wood, C. A., Lunine, J. I., et al. (2011). Regional geomorphology and history of Titan's Xanadu province. *Icarus*, *211*(1), 672–685. https://doi.org/10.1016/j.icarus.2010.07.022

Radebaugh, J., Lorenz, R. D., Ventra, D., Farr, T., Kirk, R., Lunine, J., et al. (2016). Alluvial and fluvial fans on Saturn's moon Titan reveal processes, materials and regional geology. *Journal of the Geological Society*. https://doi.org/10.1144/SP440.6

Radebaugh, Jani. (2013). Dunes on Saturn's moon Titan as revealed by the Cassini Mission. *Aeolian Research*, *11*, 23–41. https://doi.org/10.1016/j.aeolia.2013.07.001

Radebaugh, Jani, Lorenz, R. D., Kirk, R. L., Lunine, J. I., Stofan, E. R., Lopes, R. M. C., & Wall, S. D. (2007). Mountains on Titan observed by Cassini Radar. *Icarus*, *192*(1), 77–91. https://doi.org/10.1016/j.icarus.2007.06.020

Radebaugh, Jani, Lorenz, R. D., Liu, Z. Y.-C., & Kirk, R. L. (2016). The highest point on Titan. *Lunar and Planetary Science Conference XLVII*, *84602*, 46–47. https://doi.org/10.1038/ngeo2474.

Reid, R. P., Kozdon, R., Orland, I. J., Valley, J. W., Noah, J., Casaburi, G., & Foster, J. S. (2018). Fluvial geomorphology on Earth-like planetary surfaces: A review, *17*(5), 413–430.

https://doi.org/10.1089/ast.2016.1563.A

Richardson, J., Lorenz, R. D., & McEwen, A. (2004). Titan's surface and rotation: new results from Voyager 1 images. *Icarus*, *170*(1), 113–124. https://doi.org/10.1016/j.icarus.2004.03.010

Rodriguez, S., Garcia, A., Lucas, A., Appéré, T., Le Gall, A., Reffet, E., et al. (2014). Global mapping and characterization of Titan's dune fields with Cassini: Correlation between RADAR and VIMS observations. *Icarus*, *230*, 168–179. https://doi.org/10.1016/j.icarus.2013.11.017

Smith, P. H., Lemmon, M. T., Lorenz, R. D., Sromovsky, L. A., Caldwell, J. J., & Allison, M. D. (1996). Titan's Surface, Revealed by HST Imaging. *Icarus*, *349*(119), 336–349.

Solomonidou, A., Coustenis, A., Lopes, R. M. C., Malaska, M. J., Rodriguez, S., Drossart, P., et al. (2018). The Spectral Nature of Titan's Major Geomorphological Units: Constraints on Surface Composition. *Journal of Geophysical Research: Planets*, *123*(2), 489–507. https://doi.org/10.1002/2017JE005477

Solomonidou, Anezina, Bampasidis, G., Hirtzig, M., Coustenis, A., Kyriakopoulos, K., St. Seymour, K., et al. (2013). Morphotectonic features on Titan and their possible origin. *Planetary and Space Science*, *77*, 104–117. https://doi.org/10.1016/j.pss.2012.05.003

Stern, R. J., Gerya, T., & Tackley, P. J. (2018). Stagnant lid tectonics: Perspectives from silicate planets, dwarf planets, large moons, and large asteroids. *Geoscience Frontiers*, *9*(1), 103–119. https://doi.org/10.1016/j.gsf.2017.06.004

Stiles, B. W., Hensley, S., Gim, Y., Bates, D. M., Kirk, R. L., Hayes, A., et al. (2009). Determining Titan surface topography from Cassini SAR data. *Icarus*, *202*(2), 584–598. https://doi.org/10.1016/j.icarus.2009.03.032

Stofan, E. R., Elachi, C., Lunine, J. I., Lorenz, R. D., Stiles, B., Mitchell, K. L., et al. (2007). The lakes of Titan. *Nature*, *445*(7123), 61–64. https://doi.org/10.1038/nature05438

Stofan, E.R., Lunine, J. I., Lopes, R., Paganelli, F., Lorenz, R. D., Wood, C. A., et al. (2006). Mapping of Titan: Results from the first Titan radar passes. *Icarus*, *185*(2), 443–456. https://doi.org/10.1016/j.icarus.2006.07.015

1038 Stofan, Ellen R, Wall, S. D., Stiles, B. W., Kirk, R. L., West, R. D., & Callahan, P. S. (2008). Cassini
1039 Radar Users Guide. *JPL User Guide*.
1040 Tewelde, Y., Perron, J. T., Ford, P., Miller, S., & Black, B. (2013). Estimates of fluvial erosion on
1041 Titan from sinuosity of lake shorelines. *Journal of Geophysical Research E: Planets*, *118*(10),
1042 2198–2212. https://doi.org/10.1002/jgre.20153
1043 Tobie, G., Lunine, J. I., & Sotin, C. (2006). Episodic outgassing as the origin of atmospheric methane
1044 on Titan. *Nature*, *440*(7080), 61–64. https://doi.org/10.1038/nature04497
1045 Tokano, T. (2010). Relevance of fast westerlies at equinox for the eastward elongation of Titan ' s
1046 dunes. *Aeolian Research*, *2*(2–3), 113–127. https://doi.org/10.1016/j.aeolia.2010.04.003
1047 Tomasko, M. G., Archinal, B., Becker, T., Bézard, B., Bushroe, M., Combes, M., et al. (2005). Rain,
1048 winds and haze during the Huygens probe's descent to Titan's surface. *Nature*, *438*(7069), 765–
1049 778. https://doi.org/10.1038/nature04126
1050 Twidale, C. R. (2004). River patterns and their meaning. *Earth-Science Reviews*, *67*(3–4), 159–218.
1051 https://doi.org/10.1016/j.earscirev.2004.03.001
1052 Werynski, A., Neish, C. D., Gall, A. Le, & Janssen, M. A. (2019). Compositional variations of Titan's
1053 impact craters indicates active surface erosion. *Icarus*, *321*(September 2018), 508–521.
1054 https://doi.org/10.1016/j.icarus.2018.12.007
1055 Williams, D. A., Radebaugh, J., Lopes, R. M. C., & Stofan, E. (2011). Geomorphologic mapping of
1056 the Menrva region of Titan using Cassini RADAR data. *Icarus*, *212*(2), 744–750.
1057 https://doi.org/10.1016/j.icarus.2011.01.014
1058 Witek, P. P., & Czechowski, L. (2015). Dynamical modelling of river deltas on Titan and Earth.
1059 *Planetary and Space Science*, *105*, 65–79. https://doi.org/10.1016/j.pss.2014.11.005
1060 Wood, C. A., Lorenz, R., Kirk, R., Lopes, R., Mitchell, K., & Stofan, E. (2010). Impact craters on
1061 Titan. *Icarus*, *206*(1), 334–344. https://doi.org/10.1016/j.icarus.2009.08.021
1062 Zebker, H. A., Stiles, B., Hensley, S., Lorenz, R., Kirk, R. L., & Lunine, J. (2009). Size and Shape of
1063 Saturn's Moon Titan. *Science*, *324*(5929), 921–923. https://doi.org/10.1126/science.1168905

1064